Advanced Functional Materials

ADVANCED FUNCTIONAL MATERIALS
www.afm-journal.de

RESEARCH ARTICLE OPEN ACCESS

Resolving the Cu(bdc) Conundrum: Identifying Non-Porous Packing of Prototypical Coordination-Network Thin Films Combining Advanced Diffraction Techniques and Computational Modelling

Narges Taghizade[1] | Mario Fratschko[1] | Robbin Steentjes[1] | Mercedes Linares-Moreau[2] | Paolo Falcaro[2] | Christof Wöll[3] | Roland Resel[1] | Egbert Zojer[1]

[1]Institute of Solid State Physics, Graz University of Technology, NAWI Graz, Graz, Austria | [2]Institute of Physical and Theoretical Chemistry, Graz University of Technology, Graz, Austria | [3]Institute of Functional Interfaces (IFG), Karlsruher Institut für Technologie (KIT), Karlsruhe, Germany

Correspondence: Roland Resel (roland.resel@tugraz.at) | Egbert Zojer (egbert.zojer@tugraz.at)

Received: 9 January 2026 | **Revised:** 13 April 2026 | **Accepted:** 15 May 2026

Keywords: ceramic-to-MOF growth | Cu(bdc) | DFT simulation | fourier-transform infrared spectroscopy | grazing incidence X-ray diffraction | layer-by-layer growth | metal-organic framework | thin film structure solution

ABSTRACT

The functional properties of metal-organic framework (MOF) thin films crucially depend on their structure, which is often difficult to determine. A widely investigated material is Cu(bdc) (bdc = benzene-1,4-dicarboxylic acid) grown from solution, for which various thin-film structures have been suggested. Unfortunately, none of them represents a (meta)stable polymorph and is simultaneously consistent with the material's ferromagnetic nature, the difficulty of loading guest molecules, and the available diffraction data. This conundrum is resolved by combining evidence from rotating grazing-incidence X-ray diffraction, X-ray reflectivity, infrared absorption, and spin-polarized simulations. The experimental data are collected for thin films grown by layer-by-layer and ceramic-to-MOF conversion techniques. It is unambiguously shown that both samples consist of a non-porous coordination network with $Cu_2(OH)_2(bdc)$ stoichiometry with densely packed Cu^{2+}/OH^- layers connected by bdc linkers. X-ray reflectivity data confirm the dense nature of the films, and infrared spectroscopy supports the presence of additional OH^- groups. A hitherto unknown polymorph is identified as the only structure consistent with all data. For this structure, spin-polarized calculations predict a ferromagnetic ground state, in line with previous experiments. This shows that for identifying the structure of a MOF-type thin film, one has to think outside the box, combining data from complementary approaches.

1 | Introduction and Overview of the Hitherto Suggested Structures of Cu(bdc)

Metal-organic frameworks (MOFs) are chemically and structurally versatile materials suitable for various applications [1]. The tunable structure and the permeability of the pore network are critical for their application in gas storage [2], catalysis [3], drug delivery [4], and sensing [5]. In fact, most of these applications rely on the high porosity of MOF crystals [6] and on how specific building blocks are arranged relative to each other. Consequently, it is important to have an accurate knowledge of structural details when the material is used for functional

Narges Taghizade and Mario Fratschko contributed equally to this work.

applications. In this context, the progress of MOF-based device fabrication is strongly linked to the development of robust protocols for the preparation of MOF films with precisely tuned crystalline structures [7].

A prototypical MOF used for the fabrication of films and related devices is MOF-2 [8]. It consists of planar sheets with a four-fold arrangement of the linker molecules around the metal nodes [9]. The nodes consist of paddle-wheels (PWs) containing Zn^{2+} dimers connected by four benzene-dicarboxylate (bdc) ligands. Each bdc linker coordinates to two paddle-wheel units. Thus, 2D sheets are formed that are held together by robust coordination bonds. The paddle-wheels are saturated by H_2O molecules, and the originally reported structure hosts solvent molecules stemming from the synthesis. The respective crystal structure of MOF-2 is available via the Cambridge Structural Database (CSD) by the refcode GECXUH.

Also, Cu^{2+}-based MOFs with bdc linkers exist and have been employed as versatile framework systems. In fact, copper PWs connected via bdc are of notable significance due to their successful use for the fabrication of functional thin-film structures and patterns [9–11]. The contributions of Cu(bdc) to the progress in MOF research range from fundamental studies in interpenetrated frameworks [9] to molecular sieve devices for separation [12]. For optoelectronics, Cu(bdc) allows for a precise control over dye molecule orientation, making this platform material valuable for optical applications, including sensing [13] and microelectronics [10]. Additionally, its low-temperature ferromagnetism makes it relevant for spintronics and data storage due to its unique magnetic properties in quasi-1D copper ion chains [14]. Furthermore, Cu(bdc) has been applied to study magnetic coupling, offering insights into molecular-level magnetism and potential applications as quantum materials [15].

Cu(bdc)-based thin films—often referred to as $Cu_2(bdc)_2$, MOF-2, or SURMOF-2 – are frequently modelled as a P4-stacked network with open 1D square channels [9] similar to extended Cu(bdc) crystals. Yet, post-synthetic infiltration of guests is typically inefficient, and framework loading is commonly achieved only during film growth. This appears consistent with compact or blocked architectures rather than a permeable channel network. Moreover, the pronounced water stability observed for Cu(bdc) films [16, 17] contrasts with calculations showing that water destabilizes the P4 stacking [9]. This suggests the presence of a non-porous phase in Cu(bdc) thin films.

In view of the above-mentioned findings, two important questions arises: do the studied Cu(bdc) thin films share the bulk MOF-2 structure, and do they actually reproduce the bulk materials' functional properties (e.g., regarding magnetic behavior, optical alignment, mass transport, and chemical stability)? The situation is further complicated by the observation that the bulk structure formed from Cu^{2+} ions and bdc molecules is not unique: there are at least three additional structures comprising Cu^{2+} pairs linked by bdc units listed in the CSD. These are denoted as ZUBKEO [18], MUMBUU [19], and KAKSUL [20] (see Figure 1). The structures of ZUBKEO and MUMBUU are similar to the MOF-2 structure, but ZUBKEO misses the H_2O molecules saturating the Cu^{2+} ions and the solvent molecules in the pores. Interestingly, the ZUBKEO structure has been clearly identified for Cu(bdc) films grown from the vapor phase by molecular layer deposition [21], but up to now, to the best of our knowledge, not for films grown from solution [22]. Similar to MOF-2, ZUBKEO comprises pores extending perpendicular to the Cu(bdc) layers. The resulting high porosity is responsible for the comparably low densities of 1.38 and 1.53 $g.cm^{-3}$ for ZUBKEO and MUMBUU, respectively [18, 19]. In contrast, the KAKSUL structure consists of 2D extended layers of Cu^{2+} ions connected by OH^- groups (one per Cu^{2+} ion). The deprotonated bdc linkers are then bonded to these layers, as shown in Figure 1 [11]. Notably, the KAKSUL structure is non-porous, which results in a significantly increased density of 2.49 $g.cm^{-3}$ [20].

Adding to the complexity, two additional non-porous coordination networks composed of Cu^{2+} ions, bdc, and water molecules have been reported [23]. These structures, listed in the CSD as KEQTEF and JIBFUV, are illustrated in Figure S1. In KEQTEF, the copper atoms form a two-dimensional zig-zag network bridged by water molecules, with the layers further linked axially through bdc linkers. In contrast, JIBFUV features one-dimensional linear chains of Cu atoms also connected by water molecules, which are coordinated to bdc linkers.

The diversity of suggested Cu(bdc) structures does not end here, as numerous other variants of Cu(bdc) thin-film structures have been proposed. In 2012, J. Liu et al. synthesized a thin, surface-anchored MOF (SURMOF) film with a structure referred to as SURMOF-2 [9], which was suggested to be analogous to MOF-2, albeit without solvent and water molecules. Thus, SURMOF-2 is built from planes of PWs linked by orthogonal lines of bdc molecules. The suggested SURMOF-2 structure closely resembles the ZUBKEO framework discussed above, albeit with two key differences: first, in the Cu(bdc) planes in SURMOF-2, adjacent linkers are oriented orthogonal to each other, in contrast to ZUBKEO, where the linkers intersect at 93.6° and 86.4°, respectively; second, the SURMOF-2 model assumes an idealized, eclipsed stacking of successive layers, disregarding the lateral shift between Cu(bdc) planes characteristic of the ZUBKEO structure (see Figure 1). As a consequence, the proposed SURMOF-2 structure has P4 symmetry, which is higher than the P2 symmetry of bulk MOF-2 [18, 24, 25].

A complication with the SURMOF-2 structure is that it is inconsistent with the observed magnetic properties of Cu(bdc) films: ferromagnetic order was observed in Cu(bdc) thin films [14, 15], a finding that contradicts the presence of intact Cu^{2+} paddlewheels, which are known to have an antiferromagnetic singlet ground state [26, 27]. Friedlander et al. [14], therefore, proposed a framework composed of "semi-paddle-wheel" (SEMI-PW) units that are connected, such that they form zipper-like one-dimensional chains of Cu^{2+} ions; the calculations in [14] indeed indicated ferromagnetic coupling within each paddle-wheel. Notably, the SEMI-PW model is highly porous and accommodates water molecules in addition to the Cu^{2+} centers and deprotonated bdc linkers.

An alternative approach was pursued by Baumgartner et al. [28]: they used polarization-dependent Fourier-transform infrared (FTIR) spectroscopy to analyze the Cu(bdc) thin-film structure. The FTIR data suggested that bdc linkers are parallel to the film surface, such that the observed differing dichroic

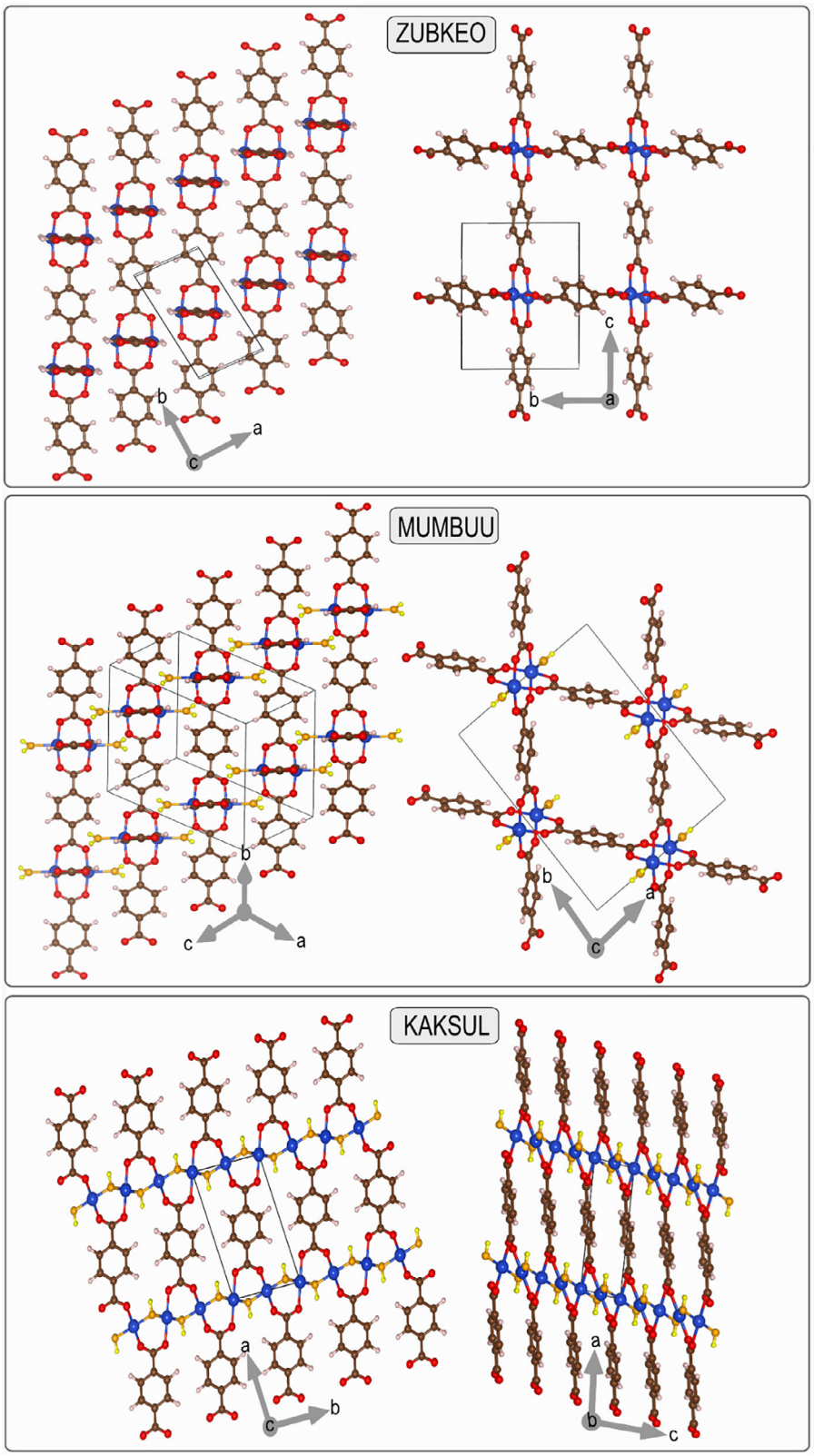

FIGURE 1 | Top and side views of different variants of Cu(bdc) structures, as documented in the Cambridge Structural Database. The plots are aligned such that at least part of the bdc-linkers run vertically. In viewing direction, the displayed structures are always one unit cell thick, while perpendicular to the viewing direction, supercells are shown. Atoms are color-coded: carbon (brown), copper (blue), oxygen (red), and hydrogen (white). In hydroxyl (OH) groups and water molecules (H_2O), oxygen atoms are highlighted in orange, and hydrogen atoms in yellow to distinguish them from the respective atoms in other chemical environments.

ratios of carboxylate stretches appeared incompatible with the classical paddle wheel configuration [28]. These discrepancies indicate a different Cu(bdc) structure, likely involving alternative coordination bonds between copper and carboxylate groups, resembling those in Cu(II) terephthalate coordination networks and Cu(II) hydroxy-terephthalate networks [23]. Additionally, the COO vibrational bands in the IR spectra suggest a denser, layered structure rather than an open 3D framework [29].

Combining the insights from the XRD and IR studies, thus, implied that Cu(bdc) thin films adopt a more complex bonding pattern than the typical 2D coordination models [28]. The situation is further complicated by the observed influence of the deposition technique used to grow the films. For example, differences were observed when comparing vapor-phase and liquid-phase growth: Rubio-Giménez et al. [22] demonstrated that reacting a $Cu(OH)_2$ precursor with bdc linkers in the vapor phase leads to the formation of the known ZUBKEO structure, while combining bdc in the liquid phase with copper hydroxide resulted in thin films with a yet unknown crystalline structure.

To unambiguously determine the crystal structure of our Cu(bdc) thin films, we applied several complementary techniques. (i) Films were prepared by two distinct solution-based fabrication methods (see also Methodology section and references cited there): ceramic-to-MOF conversion (CtM), which forms the film in a single immersion step of $Cu(OH)_2$ nanobelts into the precursor solution, where they are partly consumed; and layer-by-layer deposition (LbL), during which the metal precursor solution (Cupric acetate monohydrate) and the linker solution are alternately spin-coated onto the Si substrate and rinsed with pure ethanol between the spinning cycles. In analogy to the situation described in [30], for the LbL samples we studied films directly grown on a pristine Si substrate as well as on a substrate coated with an Au film and functionalized with a carboxylate-terminated 16-mercaptohexadecanoic acid self-assembled monolayer (SAM). For the two substrates, equivalent results were obtained. Thus, in the main manuscript, only data for the film on the pristine Si substrates are shown (which do not display additional diffraction features due to the Au layer); data for the SAM-pretreated substrates are compared in Figure S17.

The two aforementioned techniques are particularly relevant for thin-film fabrication [9, 10, 14, 31–33], as the CtM approach allows the fabrication of highly oriented, heteroepitaxially grown films [10, 32], while the LbL approach is the predominant deposition method for thin-film preparation [9, 14, 31, 33]. (ii) To determine the crystal structure of the thin films, rotating grazing incidence X-ray diffraction (rotating-GIXD) experiments [34] were performed. This approach has the distinct advantage that—irrespective of the film thickness—it allows the sampling of the majority of reciprocal space in a single experiment. This provides a much more complete picture of the sample´s structure compared to measurements limited to specific planes within the reciprocal space (e.g., by in-plane and out-of-plane diffraction experiments). Moreover, rotating-GIXD data also allow an unambiguous determination of the film texture via the extraction of pole figures [29, 35]. The full potential of this technique for determining MOF structures has been discussed in two recent studies [29, 35]. (iii) To identify whether one is dealing with highly porous or with densely packed films, X-ray reflectivity (XRR) measurements were performed, which allow determining the total electron density of a thin film sample [36]. (iv) The presence of certain functional groups was checked by Fourier transform infrared absorption spectroscopy (FTIR). (v) Finally, state-of-the-art dispersion-corrected density-functional theory (DFT) simulations were used to optimize atomic positions and unit cells of potential candidate structures. This allows comparing the hypothetical diffractograms of simulated structures to experimental data. Moreover, simulations can be applied to refine and test structural models, which are generated from the measured data, and to test the stability of specific structures. A crucial strategy in this context is to fully optimize not only atomic positions but also all lattice parameters of candidate structures, an aspect in which the current study deviates from the bulk of the existing literature on modelling MOF thin-film structures.

Combining the individual pieces of the puzzle, it is eventually possible to identify the true structure of Cu(bdc) for the two types of films studied here.

2 | Results and Discussion

2.1 | Comparing the Phases of the Layer-by-Layer and Ceramic-to-MOF Grown Samples

As a first step, we examined whether the Cu(bdc) samples grown with LbL and CtM techniques display the same crystal structures. Figures 2a–c display typical reciprocal space maps collected from the two films. For the LbL sample, the map integrated over the azimuthal angle is shown, as for this film, we do not observe changes in the GIXD patterns as a function of the sample rotation. In contrast, for the CtM sample, the results obtained for scattering vectors in a plane perpendicular to the preferential [100] direction of the $Cu(OH)_2$ nanobelts (q_x, q_z) and in a plane parallel to that direction (q_y, q_z) are shown.

Comparing the reciprocal space maps for the two samples reveals certain similarities, but also pronounced differences: The sample grown by the LbL method displays diffraction peaks that are elongated into arc-type structures, indicative of a notable out-of-plane mosaicity (Figure 2a). This suggests a preferred orientation of the crystallites relative to the substrate normal, yet with a distribution of tilt angles rather than a perfectly aligned texture. In contrast, the diffractograms for the CtM sample depend on the azimuthal orientation of the sample, which already indicates a more anisotropic in-plane organization. This is due to a pronounced texture of the $Cu(OH)_2$ nanobelts resulting from the chosen preparation method: [10, 32] the long axes of the nanobelts are uniaxially aligned together with a (weak) preferred orientation of the nanobelt surface parallel to the silicon substrate [35]. Accordingly, two reciprocal space maps are shown to provide a more comprehensive characterization: in the q_x/q_z map, only Debye-Scherrer rings are observed (Figure 2b), while in the q_y/q_z plane, diffraction peaks broadened into arc-like structures can be resolved (Figure 2c). The widths of these arcs are larger than in Figure 2a. Notably, the radii of the rings and arcs in panels *b* and *c* are identical (i.e., they correspond to identical lengths of the scattering vector q), but the intensity distributions are different. In addition to the diffraction features associated with Cu(bdc), the CtM sample also shows a reflection expected for the $Cu(OH)_2$

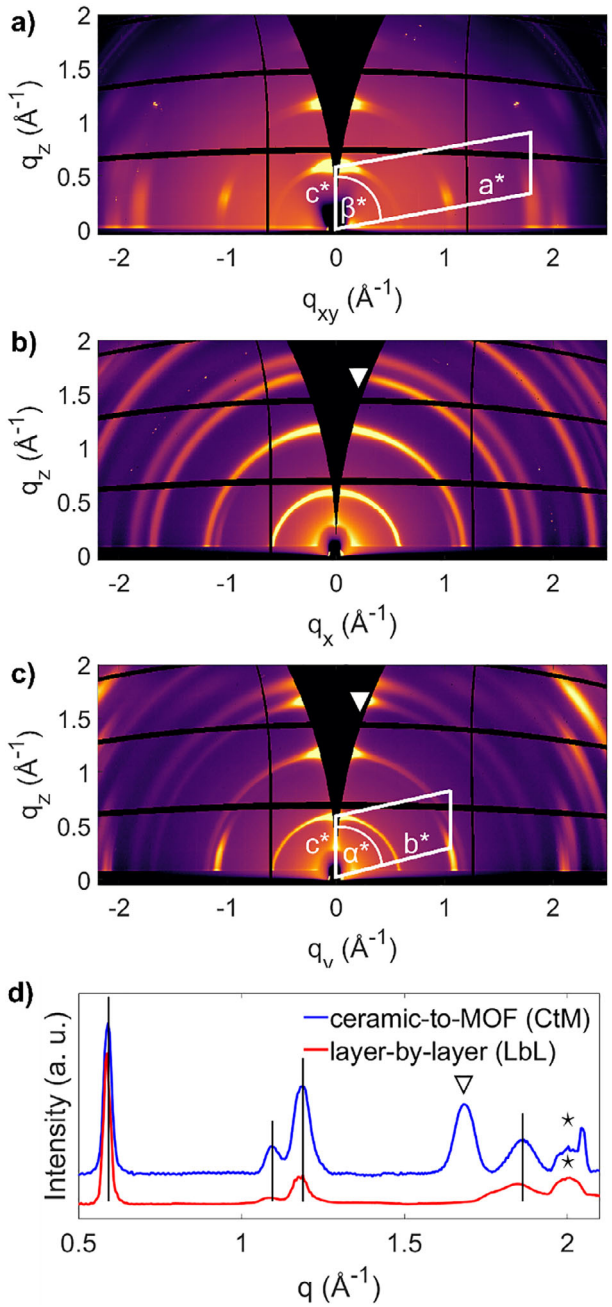

FIGURE 2 | Reciprocal space maps of Cu(bdc) thin films grown with a) the layer-by-layer (LbL) technique on a native silicon (100) substrate and (b,c) with the ceramic-to-MOF (CtM) technique on $Cu(OH)_2$ nanobelts. The data in panel (a) have been integrated over all azimuthal angles (see main text), while the GIXD map in panel (b) corresponds to the q_x/q_z plane, that is, a plane in reciprocal space perpendicular to the preferential [100] direction of the nanobelts. In contrast, the q_y/q_z plane in panel (c) is parallel to that direction. The parallelograms in (a) and (c) represent the crystallographic unit cell within the reciprocal lattice of the Cu(bdc) crystal structure that are obtained by indexing of the GIXD data, as described in Section 2.5. (d) Quasi-powder pattern generated from the rotating-GIXD measurement of the two thin films prepared by the CtM (blue) and LbL techniques (red). The stars indicate the silicon 111 Bragg peak of the underlying silicon substrates for both samples. For the CtM sample, the triangle highlights additionally the 021 Bragg peak of the $Cu(OH)_2$ nanobelt precursor. The vertical full lines denote the peak positions associated with the Cu(bdc) crystal structure.

nanobelts at q = 1.696 Å^{-1} [37, 38]. This feature appears as a Debye-Scherrer ring in the q_x/q_z plane and as a Bragg peak broadened into an arc-shaped structure in the q_y/q_z plane. Its position is highlighted in Figures 2b and c by the filled white symbol "∇". The qualitatively similar shapes of the diffraction features for Cu(bdc) and the nanobelts suggest that the orientation of the Cu(bdc) domains is influenced by the alignment of the underlying. This is nanobelts, consistent with our previous observations for MOFs comprising Cu(bdc) layers spaced by 1,4-diazabicyclo [2.2.2] octane (dabco) linkers [35].

The experimental observations described above raise the question of whether the two samples consist of different Cu(bdc) phases or whether in the LbL and CtM samples one is dealing with crystallites with identical structures but fundamentally different textures. To clarify that, quasi-powder patterns were calculated from the rotating-GIXD data. These are shown in Figure 2d. When disregarding substrate-related peaks (denoted by "∇" and "*"), it turns out that the peaks in the quasi-powder patterns of the LbL and CtM samples are at exactly the same positions. Variations in intensities of quasi-powder patterns cannot be compared directly, as explained in the Methods section. Therefore, the data in Figure 2d indicate that both samples display the same crystal structure. Notably, the two quasi-powder patterns are comparable in terms of peak positions (q = 0.59, 1.09, 1.18, and 1.86 Å^{-1}) and peak intensities to a powder pattern from randomly distributed Cu(bdc) crystals [14].

The fundamentally different textures of the films will become relevant in Section 2.3. Before that, the quasi-powder patterns will be used as a first tool to find evidence, for whether hitherto suggested structures for Cu(bdc) thin films are consistent with the samples studied here.

2.2 | Phase Analysis Based on the Quasi-Powder Pattern of the CtM Sample

As a first step, to rule out crystallographic phase(s) that do not dominantly occur in the studied samples, simulated powder patterns of plausible Cu(bdc) structures are compared to the quasi-powder GIXD pattern of the CtM thin film. The latter is representative of the types of thin films studied here, as discussed in the previous section. Figure 3 compares the quasi-powder pattern of the CtM sample to the expected peak positions of the possible structures discussed in the Introduction. For the sake of clarity, the peaks are not indexed. To ease the comparison between the simulated and measured patterns, the main peaks in the latter are highlighted by vertical grey bars labeled by Roman numbers (I–IV). A list of all possible candidate structures is given in the Supplementary Information, Table S1. The grey bars in Figure 3 allow phase identification based on peak positions, enabling a direct visual match between experiment and simulation.

Importantly, in the following, we will, on the one hand, consider simulations in which the lattice parameters and the atomic positions were relaxed simultaneously. In these cases, lattice parameters extracted from experiments were only used as the starting structures for the geometry optimizations. This allows an assessment of whether a specific set of lattice parameters

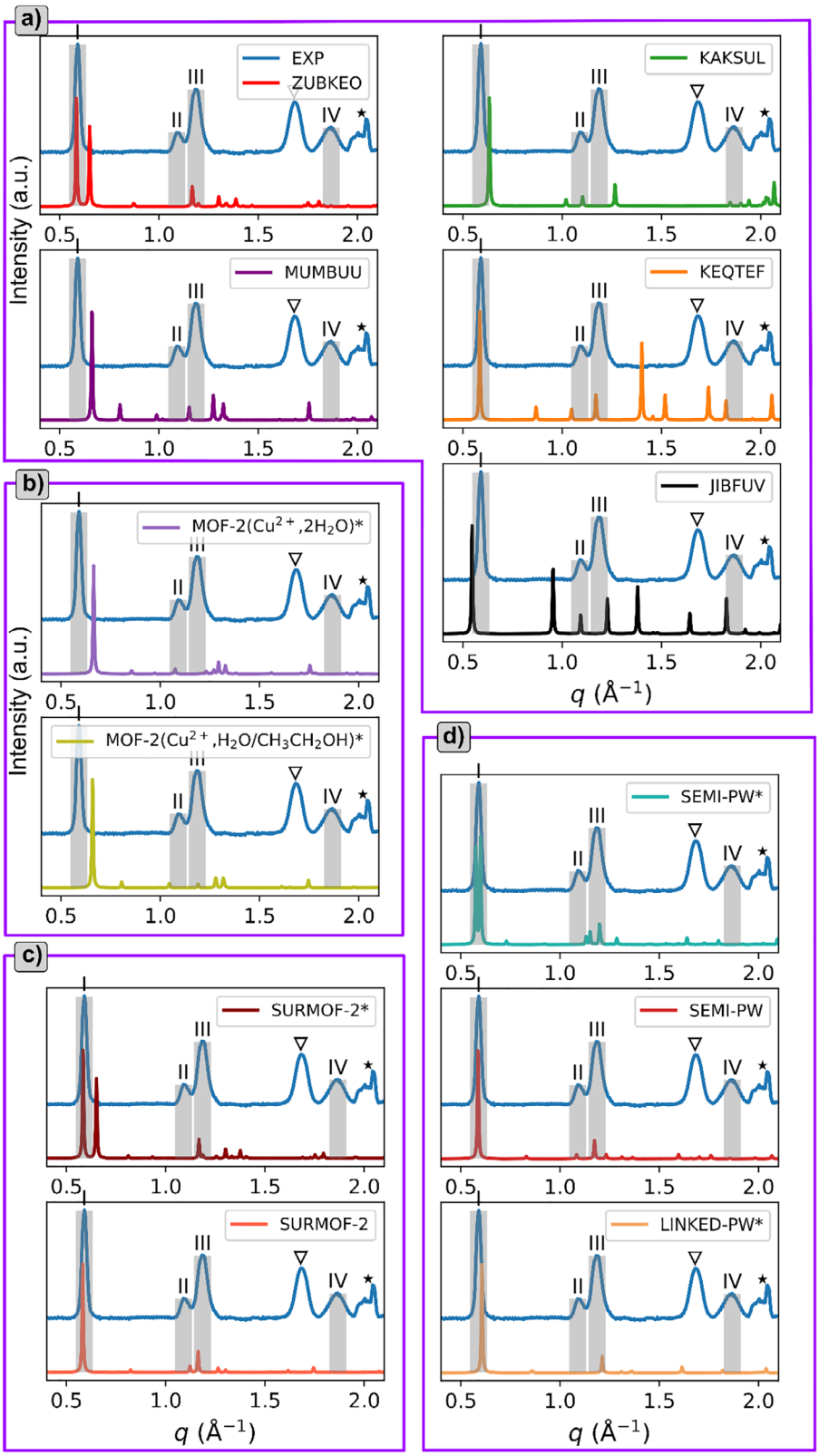

FIGURE 3 | Comparison between (quasi-)powder X-ray diffraction patterns (c.f., Method section) of the thin film prepared via the ceramic-to-MOF method (blue line in all panels) and various possible variants of Cu(bdc) structures inspired by literature, as described in the main text. Panel (a) compares the experimental features with simulated powder patterns for Cu(bdc) structures from the CSD, (b) considers MOF-2 derived structures, (c) provides a comparison with SURMOF-2 type structures, and (d) illustrates the situation for SEMI-PW structures. The vertical grey bars highlight the four most significant experimental peaks of Cu(bdc). The peak marked with a triangle originates from the $Cu(OH)_2$ nanobelts remaining after MOF synthesis, while the star denotes the 111 peak of the silicon substrate. Fully optimized structures are denoted by an asterisk after the name, while for the other structures only atomic positions have been optimized, and lattice parameters have been taken from experiments.

represents a stable configuration, and one avoids the misleading impression that a simulation appears consistent with an experimental result in cases in which the agreement has been enforced extrinsically. Such fully optimized structures will be denoted by an asterisk after the name of the structure (like, for example, SEMI-PW*). On the other hand, there are certain instances in which it is still useful to fix lattice parameters at experimental values. This, for example, applies to structures directly extracted from the CSD. These only partially optimized structures will be denoted by their bare names and CSD refcodes (like KAKSUL).

Figure 3a shows that when calculating diffractograms based directly on the structures of Cu(bdc) variants reported in the CSD, no satisfactory agreement with the experimental data is observed: for the layered ZUBKEO structure, there are two peaks at lower q, while in the experiments, there is only one (peak I). Moreover, no diffraction maxima correspond to the experimental features II and IV. In the case of MUMBUU, there is some correspondence between the experiment and the simulation in the region of peak III, but no agreement is found for peaks I and II. For the densely packed KAKSUL structure, none of the experimental features overlaps with a calculated diffraction peak. This might appear somewhat surprising, as the Zn^{2+}-analogue of the (Cu^{2+}-based) KAKSUL has recently been unambiguously identified in Zn(bdc) type thin film structures grown by the LbL technique at certain precursor concentrations [30]. Still, the structure apparently does not appear in the studied Cu(bdc) thin films. For the KEQTEF structure, experimental features perfectly match peaks I and III; however, multiple rather strong simulated diffraction features are missing in the experiments. Finally, for the JIBFUV structure, the agreement is worst, as only the experimental feature II matches a simulated peak. Additionally, multiple strong peaks appearing in the simulations are not found in the experiments. Taken together, these mismatches indicate that none of the indexed CSD Cu(bdc) polymorphs can account for the four main experimental features (I–IV) observed for the CtM (and, as discussed in the previous section, also for the LbL) films. This shows that bulk structures cannot necessarily be directly applied to thin films.

As a next step, alternative plausible structures were tested, for which (to the best of our knowledge) no perfectly suited single-crystal data are available, at least for the Cu^{2+} variants of the MOF: One of them is based on the Zn^{2+} based structure of MOF-2, in which the Zn^{2+} ions are saturated by H_2O molecules and dimethylformamide (DMF) solvent molecules are contained in the pores. This structure is referred to as GECXUH in the CSD [24]. For this system, the Zn^{2+} ions were replaced by Cu^{2+} ions, DMF was removed, and the resulting structure was optimized, including the lattice parameters. This yields a structure referred to as MOF-2(Cu^{2+}, $2H_2O$)*. In a second test system, one of the H_2O molecules was replaced by an ethanol molecule, yielding MOF-2(Cu^{2+}, H_2O/CH_3CH_2OH)*. Further details on these structures are provided in the Supporting Information, Table S2. As shown in Figure 3b, these structures also do not yield powder patterns consistent with the experiments, indicating that MOF-2-based structures are not found in the Cu(bdc) thin films studied here. This suggests that simple cation substitution of the known Zn-MOF-2 metrics is insufficient to provide an accurate description of the CtM film structure.

Another possible structural motif would be SURMOF-2, suggested for Cu(bdc) thin films grown via the LbL approach [8]. This structure does not contain any H_2O molecules saturating the Cu^{2+} ions and assumes a square arrangement of the paddle wheels in the plane in which they are connected by the bdc linkers (see Figure S2). Notably, in a full geometry optimization, this structure is not stable, and the high-symmetry conformation assumed for SURMOF-2 does not prevail. Rather, in the fully optimized variant of the SURMOF-2 motif (here referred to as SURMOF-2*), consecutive layers shift, as illustrated in Figure S2 and Table S3. This yields a diffraction pattern that does not bear much resemblance to our experiments. Especially, the splitting of the main diffraction peak into two peaks due to the symmetry breaking is not observed in the experiments (see Figure 3c). In fact, a more in-depth analysis of the structure of the fully optimized SURMOF-2 motif, including the construction of the associated Niggli cell [39], reveals that it corresponds to the ZUBKEO structure from the CSD already discussed above (only with a differently chosen unit cell; see Supporting Information Table S3 and Figure S3). Accordingly, the top left panels in Figure 3a and c are identical.

The above-mentioned splitting of the first peak (corresponding to the (100) and (010) features) would, however, disappear if the slips of consecutive layers occurred in opposite directions. This could be a realistic scenario [40], as has been discussed in detail for layered covalent organic frameworks [41]. Moreover, the SURMOF-2 structure is a thin-film structure and, thus, could, in fact, represent a substrate-induced phase [42] (which might be unstable in bulk simulations). Therefore, a SURMOF-2 structure with fixed lattice parameters was also considered (see Figure S2). In this case, only the positions of the individual atoms were optimized. In Figure 3, this structure is denoted as SURMOF-2. The resulting diffractogram bears some resemblance to the experimental data (see Figure 3c). In fact, the first peak of SURMOF-2 overlaps with peak I of the experiments, there is a weak feature reasonably close to peak II, and a stronger one close to peak III. Only for peak IV, the shift between experimental peak positions and calculated diffraction features is larger. This seeming reasonable agreement, however, needs to be taken with a grain of salt: finding an agreement with an experiment, when using lattice parameters extracted from a similar experiment (here, lattice constants extracted from in-plane and out-of-plane diffraction experiments), is not really conclusive. Thus, it will be necessary to further assess the appropriateness of the SURMOF-2 structure below when going beyond a mere comparison of quasi-powder patterns.

A further complication with the "traditional" SURMOF-2 structure (independent of whether lattice parameters are optimized or not) is that its magnetic properties are inconsistent with the experimentally observed ferromagnetic alignment of the spins of the Cu^{2+} ions, as reported by Friedlander et al. [14] and Nefedov et al. [15]. Thus, in ref. [14] an alternative "semi-paddle wheel" structure has been suggested, comprising 1D chains of Cu^{2+} ions linked in a zipper-like fashion. This structure is visualized in Figure S4. Notably, in our simulations, it turned out not to maintain its overall structure when relaxing the lattice parameters. Thus, we once more studied two variants: one in which lattice constants and atomic positions were fully optimized (SEMI-PW*) and one in which the lattice parameters

were set to the values extracted from experiments, assuming a "semi-paddle wheel" structural motif (SEMI-PW) [14]. The resulting calculated powder diffractograms are compared to the experimental one in Figure 3d. The fixed-parameter variant once again provides a reasonable agreement with pronounced maxima at the experimental positions of peaks I, II, and III. This is again not really surprising for the same reasons discussed above for the SURMOF-2 structure. Still, the agreement is far from perfect as there are no features in the region of peak IV. Additionally, the simulated powder pattern displays multiple peaks that are not visible in the experiments. For the fully optimized structure, the agreement with experiments deteriorates, albeit to a lesser degree than for the SURMOF-2 case. In passing, we note that, like in the SURMOF-2 case, at this stage it is not possible to rule out that the improved match for the fixed-metric SEMI-PW structure is again a consequence of the impact of the substrate (which is not accounted for in the simulations).

As a further plausible case, based on the SURMOF-2 and SEMI-PW structures, we constructed an "intermediate" structure referred to as LINKED-PW. In this structure, neighboring Cu^{2+} ions are directly bridged via carboxylate groups, and the orthogonal bdc linkers are shifted by one Cu-Cu spacing. This structural motif has, for example, been suggested based on simulations on SURMOF-2-related materials with more complex linkers [43]. In contrast to the SEMI-PW structures, no H_2O molecules are included along the Cu^{2+} containing chains, and all Cu^{2+} ions within the chains have identical distances (see Table S5). This structure is referred to as LINKED-PW*, and the diffractogram obtained after a full geometry optimization is shown in Figure 3d. It is rather similar to that of the SEMI-PW* structure with an overall reduced number of peaks due to the somewhat higher symmetry. Thus, it also does not match the experiments. In summary, none of the tested models fully reproduces all four principal experimental features (I–IV).

2.3 | Phase Analysis Based on Reciprocal Space Maps

Despite the aforementioned lack of perfect agreement, SURMOF-2 and the SEMI-PW structures yield calculated powder diffractograms with some resemblance to the quasi-powder pattern derived from the rotating-GIXD experiments. As discussed in the previous section, these structures do not correspond to equilibrium structures of a crystalline bulk material, but at this stage, it cannot be excluded that they might be surface-induced phases.

To test whether this is indeed the case, we resorted to the rotating-GIXD experiments, which provide a much richer set of data than the quasi-powder diffractograms. Consequently, in the following calculated GIXD data for the two aforementioned structures will be compared to the experimental rotating-GIXD measurements.

To enable this comparison, as a first step, the orientation distributions of the crystallites (the so-called textures) need to be determined. This can be done using pole figures, which can be extracted from the rotating-GIXD data at q-values at which defined diffraction peaks are observed [22, 29, 35, 44]. For the LbL and CtM thin films, this was done for $q = 0.59$ Å^{-1} and $q = 1.09$ Å^{-1} (compare Figure 2d). The resulting pole figures for both types of samples are shown in the Figures S8 and S9, together with a more in-depth discussion of their interpretation in Chapter S5.

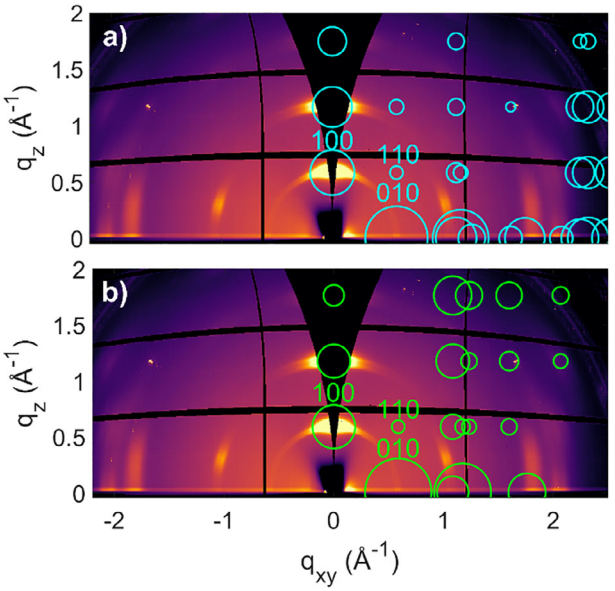

FIGURE 4 | Reciprocal space maps of Cu(bdc) prepared by the layer-by-layer method. The calculated peak patterns of (a) the SURMOF-2 structure and of (b) the SEMI-PW structure are superimposed as circles in the right half of the plots. The expected peak positions and the associated structure factors are given by the centers and the areas of the circles. Laue indices are given only for three selected diffraction peaks. Please note that for the indexing the Niggli cell has been used (c.f., Table S3), for which the paddle-wheels/Cu2$^+$ ions are stacked in a direction rather than in c direction (as sometimes chosen in literature).

In short, for the LbL samples, the pole figures reveal that there is a defined (at this stage still unknown) crystallographic plane parallel to the substrate surface, but there is no azimuthal alignment of the crystallites. Such a distribution of crystal orientations is classified as uniplanar texture [45]. In contrast, the pole figures of the CtM sample hint towards a uniaxial texture [45]. Here, the crystallites are aligned with a specific (again not yet known) crystallographic direction parallel to the substrate surface. Regarding the azimuthal orientation, this direction coincides with the [100] direction of the nanobelts. These textures also explain the specific appearance of the diffraction features in the reciprocal space map shown in Figure 2a–c. In fact, the appearance of rings for an incident x-ray beam parallel to the long axes of the nanobelts appears related to a certain degree of disorder concerning the rotation around the fiber axis (i.e., mosaicity).

Because of its uniplanar texture and more clearly resolved diffraction peaks, the LbL sample was chosen as a reference system for the direct comparison between the experimental peak positions and calculated peak patterns. For this, a specific plane of the crystal structures needs to be oriented parallel to the substrate surface. For our two remaining crystal structures (SURMOF-2 and SEMI-PW) the best agreement is obtained when choosing the (100) planes. As shown in Figure 4, in both types of structures, the agreement is very good for peaks located at q_{xy}/q_z = 0 Å^{-1}/0.59 Å^{-1} and at 0.59 Å^{-1}/0 Å^{-1}. For these peaks, Laue indices

of 100 and 010 can be assigned. However, for both structural models, the remaining calculated peaks do not coincide with experimental peak positions. As expected, similar comparisons of the GIXD data with all other structures discussed in the context of Figure 3 do not yield more promising results. For the sake of completeness, this is shown in the Supporting Information Figures S6 and S7. Also, for the CtM sample, no satisfactory agreement between experimental and simulated GIXD patterns can be achieved.

As a consequence, none of the structures considered so far provides a reasonable description of the Cu(bdc) samples grown by the LbL and CtM techniques. This shows that the traditional approach of identifying thin-film structures based either on existing bulk structures or on idealized structures suggested in literature fails for the Cu(bdc) thin films studied here. This is also a plausible explanation for why, so far, no fully convincing structure of Cu(bdc) thin films has been provided despite a rather large number of dedicated studies [9, 10, 14, 28]. For the present investigation, the negative outcome of the above comparisons means that alternative strategies have to be pursued (vide infra). In passing, we note that the current problem is different from a classical, simulation-based "crystal structure prediction challenge" [46, 47], as we, on the one hand, do not even know the actual stoichiometry of the studied thin films. This is because the relative number of bdc molecules could be reduced by incorporating -OH^- groups to maintain charge neutrality, like in the KAKSUL [20] and PUCYAO [48] structures. Alternatively, intact H_2O or solvent molecules could be incorporated to saturate bonds like in the MOF-2 structure. On the other hand, we do not have to solely rely on simulations, but have access to rotating-GIXD data that map large volumes of reciprocal space. Moreover, it is possible to acquire additional, complementary experimental information on the studied films.

2.4 | Porous vs. Densely Packed Structures

This additional information includes, for example, total electron densities, which can be obtained from the critical angles of total external reflection in X-ray reflectivity (XRR) experiments. When comparing the XRR results obtained for the films studied here to results for thin films with known crystal structures, the packing density of our Cu(bdc) films can be determined, and it can be clarified whether the films are porous or densely packed, as previously done for the ZUBKEO phase [21]. Figure 5 shows X-ray reflectivity curves for Cu(bdc) and Cu $_2$(bdc)$_2$(dabco) thin films, both prepared by the CtM technique on silicon substrates. The latter film is used as a reference material, since its crystal structure is well established and it represents a MOF with a 3D porous structure [35]. Both reflectivity curves show two intensity maxima. The maxima at lower incidence angles (α_i) are related to total external reflection of X-rays from the thin films ($Cu_2(bdc)_2(dabco)$ or Cu(bdc)). The maxima at larger α_i appear due to total reflection from the silicon substrate. A strategy for roughly estimating α_C is associating it with the angle at which the reflected intensity drops to 50% of its maximum value (mind the logarithmic intensity scale in Figure 5) [49]. A value of 0.23° is obtained for the substrate (see vertical black line). This agrees rather well with the expected value for silicon [50, 51]. Applying the same procedure to the Cu(bdc) and $Cu_2(bdc)_2(dabco)$ thin films yields the angles provided in Table 1 (for more details, see Figure S10). From these angles, the respective electron densities can be calculated using the equation provided in the Methods section.

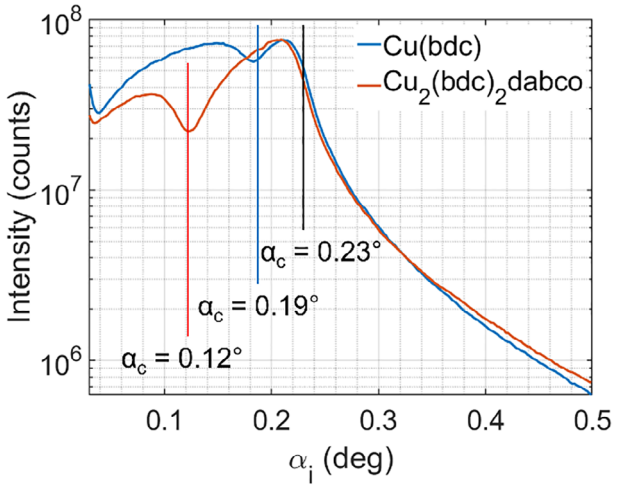

FIGURE 5 | X-ray reflectivity curves for Cu(bdc) and $Cu_2(bdc)_2(dabco)$ thin films, both prepared by the CtM method on silicon substrates. The specularly reflected intensity is plotted as a function of the incidence angle α_i. The red and blue vertical lines illustrate the positions of the critical angles for the different materials $Cu_2(bdc)_2(dabco)$ and Cu(bdc), respectively. For their identification, it is estimated at which angles the intensity of the features associated with total reflection at the thin films reaches 50% (see Figure S10). The critical angle of the silicon substrate is shown by the black vertical line.

The experiments show that the electron density in the Cu(bdc) film is 2.6 times as high as in the $Cu_2(bdc)_2(dabco)$ film. To put this into perspective, in the bottom part of Table 1, the electron density of the $Cu_2(bdc)_2(dabco)$ crystal structure taken from literature [35] is compared to the electron density of the ZUBKEO structure (consisting of stacked, porous Cu(bdc) layers) and to the densely packed KAKSUL structure (which possesses $Cu_2(OH)_2(bdc)$ stoichiometry—see introduction section). The absolute values of these electron densities do not fully match those extracted from the XRR data, which is not surprising considering the simplistic strategy for determining α_c [52]. However, the measured and calculated ratios of the electron densities tell an interesting story: When comparing the ZUBKEO structure comprising 1D extended pores (chemical composition Cu(bdc)) to $Cu_2(bdc)_2(dabco)$, the electron density increases only by a factor of 1.7. To get an increase by a factor slightly higher than the measured ratio of 2.6, one needs to resort to a non-porous variant of a Cu(bdc) structure, like KAKSUL. This is a strong indication that the Cu(bdc) films studied here are, in fact, also non-porous. This is a highly relevant input in our quest to determine the actual structure of Cu(bdc) thin films. It, however, does not yet provide a final answer, as the KAKSUL structure, as the only non-porous structure considered so far, is inconsistent with the diffraction data (see Section 2.2). Thus, it is necessary to identify an alternative, non-porous structure. To that aim, it is necessary to pursue an alternative approach and to test, whether a new structure can be identified starting directly from the GIXD data and disregarding all

TABLE 1 | First two rows: Critical angles of total external reflections α_C of Cu(bdc) and $Cu_2(bdc)_2(dabco)$ as determined from X-ray reflectivity experiments together with the resulting electron densities $\rho_{electron}$. Last three rows: Expected values for α_C and $\rho_{electron}$ derived from the crystal structure data. "ratio" refers to the ratio between the respective electron densities and the electron density of Cu(bdc)(dabco). The latter has been obtained in a reference experiment (second row) and has also been calculated for the structure taken from the CSD (last row).

		α_C [deg]	$\rho_{electron}$ [Å^{-3}]	Ratio
From XRR	Cu(bdc)	0.194	0.538	2.6
	$Cu_2(bdc)_2(dabco)$	0.120	0.206	
From CSD structure	ZUBKEO	0.173	0.414	1.7
	KAKSUL	0.223	0.712	2.9
	$Cu_2(bdc)_2(dabco)$[a]	0.131	0.247	

[a]deposition number 2391759 in the CSD.

"suspect" structures derived from the literature review provided above.

2.5 | Indexing of the Cu(bdc) Thin Film Phase

For extracting the structure directly from the GIXD data, as a first step, an indexation of the diffraction patterns is required. A complete list of all observed diffraction peaks from both samples and the procedure of indexing are provided schematically in Table S6 and Figure S11. The indexing is based on a combination of the GIXD patterns of both types of samples. In a first step, the q_y/q_z plot of the CtM sample is tentatively indexed by a 2-dimensional reciprocal lattice, as indicated by the white grid in Figure 2c. This yields the reciprocal lattice constants *b* and c**, and the angle α^*. Interestingly, exactly the same 2D reciprocal lattice has been observed in electron diffraction experiments already on a CtM sample [10], albeit without attempting to solve the actual thin-film structure further. In a subsequent step, a* and β^* need to be determined. Due to the uniaxial texture of the CtM sample, this is not possible using, for example, the q_x/q_z plot (see Figure 2b). Therefore, the q_{xy}/q_z plot of the LbL sample is used for determining a second 2D plane of the reciprocal lattice (white grid in Figure 2a). This second step of indexing is done disregarding all peaks that are already part of the first 2D plane of the reciprocal lattice assigned before. These also show up in Figure 2a due to the uniplanar texture of the LbL film. For aligning the two 2D reciprocal lattices relative to each other, the angle γ in the real space lattice is assumed to be 90°. From the reciprocal lattice, it is then straightforward to determine the real-space lattice. The lattice parameters of the resulting thin-film phase of Cu(bdc) (in the following referred to as Cu(bdc)-TF) are summarized in the central column of Table 2.

Notably, the unit-cell volume of that structure is significantly smaller than that of any of the structures tested before with the exception of KAKSUL. This is consistent with a densely packed nature of the films, as implied by the electron density determination in the previous section. This sets certain limits as to what could be contained in that unit cell. For example, the unit cell of the ZUBKEO structure contains two Cu^{2+} ions and two bdc linkers, but at a unit-cell volume that is larger by a factor of approximately 2.5 than in the present case (see Table S3). Including the same building blocks into the Cu(bdc)-TF unit cell would, thus, result in an unrealistically high mass density. Conversely, when including two Cu^{2+} ions, two OH^- groups, and only one doubl deprotonated bdc linker, like in the KAKSUL structure, this yields a mass density of 2.43 g cm^{-3}, which is extremely close to the 2.49 g cm^{-3} of KAKSUL itself. This suggests that the Cu(bdc)-TF structure might be similar, albeit not identical to the (densely packed) KAKSUL structure reported in the CSD.

2.6 | Atomistic Structure of the Cu(bdc) Thin Film Phase

Due to the limited number of diffraction peaks for the thin film samples, a determination of the positions of the atoms inside the unit cell based on the GIXD data is futile [44, 53]. Thus, again, simulations are used for optimizing the atomic positions with an initial arrangement of the atoms inspired by the KAKSUL unit cell. In a first step, the unit-cell parameters are fixed to the experimentally determined values, which yields the final Cu(bdc)-TF structure. As a second step, a full geometry optimization is performed, varying also the unit-cell dimensions. This structure is referred to as Cu(bdc)-TF*. The lattice constants of that structure are also included in Table 2. An important outcome of the full optimization is that it only marginally changes the lattice parameters compared to the ones estimated based on the experiments. This shows that the Cu(bdc)-TF* structure essentially corresponds to a true minimum on the potential-energy surface, rendering this structure much more realistic than the SURMOF-2 and the SEMI-PW structures.

The atomistic structures of Cu(bdc)-TF*, of Cu(bdc)-TF, and of KAKSUL are illustrated in Figure 6. They all share a conceptually similar packing motif: They consist of lines of Cu^{2+} ions connected by OH^- groups, with the lines arranged in planes. Perpendicular to the planes, the lines are connected by the doubly deprotonated bdc molecules. Still, there are differences, for example, in the arrangement of the Cu^{2+} ions: While they are aligned along a straight line in *b*-direction in Cu(bdc)-TF* (see Figure 6), they are assembled in a zig-zag pattern in Cu(bdc)-TF in that direction; still, one finds a close to straight arrangement of Cu^{2+} ions along a line significantly tilted relative to the *b*-axis. A similar pattern for the Cu^{2+} ions is found for the KAKSUL structure, although there, the in-plane unit-cell vectors are no longer orthogonal. The differences in the arrangements

TABLE 2 | Crystallographic and magnetic data of densely packed Cu(bdc) structures: KAKSUL from the Cambridge Structural Database (lattice constants according to Niggli criteria), the phase observed for the thin films after extracting unit-cell parameters from the rotating GIXD experiments and optimising only the atomic positions (Cu(bdc)-TF), and an analogous phase obtained by simultaneously optimizing atomic positions and unit-cell parameters (Cu(bdc)-TF*).

	KAKSUL	Cu(bdc)-TF	Cu(bdc)-TF*
a [Å]	3.48	3.43	3.47
b [Å]	6.34	6.04	5.90
c [Å]	10.14	11.23	11.20
α [deg]	98.76	105.4	105.22
β [deg]	96.57	97.9	98.74
γ [deg]	99.17	90	89.41
volume [Å^3]	216.3	222.4	218.7
composition	$Cu_2(OH)_2$(bdc)	$Cu_2(OH)_2$(bdc)	$Cu_2(OH)_2$(bdc)
Z	1	1	1
Energy [meV]	567	395	0
Magnetic ground state	AFM	AFM	FM

of the Cu^{2+} ions coincide with differences in the positions of neighboring O atoms belonging to the OH^- groups and to the bdc linkers. These occur despite the rather similar unit cells.

Overall, the finding that in the simulations Cu(bdc)-TF* has a distinctly lower energy than KAKSUL implies that the former is the actual minimum structure of densely packed Cu(bdc), not only for thin films, but also in the bulk. In view of the clearly lower energy of Cu(bdc)-TF* compared to Cu(bdc)-TF, the Cu(bdc)-TF* structure can be considered as the final thin-film structure found in the present study by our combined theoretical and experimental approach. This notion is supported by our observation that a full geometry optimization starting from the KAKSUL structure ends in the Cu(bdc)-TF* structure (for details see Supporting Information: Section S6.3).

Interestingly, the different relative alignment of Cu^{2+} and OH^- ions illustrated in the bottom panels of Figure 6 also impacts the coupling of the unpaired spins on the Cu^{2+} ions: while within the primitive unit cell, they adopt an antiparallel alignment (i.e., an antiferromagnetic coupling) for the KAKSUL and for Cu(bdc)-TF, they are aligned parallel for Cu(bdc)-TF*. That is, in the latter system the spins are ferromagnetically coupled. The relative energetics of the different spin configurations are detailed in Table S8, and the lowest-energy spin state is also specified in Table 2. Notably, the ferromagnetic coupling in Cu(bdc)-TF* also unambiguously prevails when considering a supercell containing four Cu^{2+} ions along the lines running in *b*-direction (see Supporting Information: Section S6.4). This observation is insofar relevant, as Friedlander et al. found Cu(bdc) thin films to be ferromagnetic [14] in electron paramagnetic resonance (EPR) experiments combined with magnetization studies. In passing, we note that the reason why Cu(bdc)-TF* displays a ferromagnetic coupling is provided by the Goodenough-Kanamori rules. These rules describe how the superexchange interaction between transition metal ions is mediated by ligands. The magnetic coupling depends on the bond angle and on the overlap between the metal d-orbitals and ligand p-orbitals. Specifically, ferromagnetic coupling is found in cases in which the bond angle deviates significantly from 180° (just as it is the case in Cu(bdc)-TF*) [54–57].

2.7 | Structure Verification

As a final step, the DFT-optimized structures of Cu(bdc) are verified against the experimental data. First, the 2D reciprocal space map obtained in the GIXD experiment for the LbL sample is compared to the calculated peak pattern (see Figure 7a). The peak pattern is obtained by choosing the (001) plane of the Cu(bdc) crystals to be parallel to the substrate surface. A perfect agreement of 001 and 002 reflections with experimental peak positions is found. The arc-type character of the peaks is attributed to an out-of-plane mosaicity of the Cu(bdc) crystals. The experimental peak intensity at q_{xy}/q_z = 1.042 Å^{-1}/0.301 Å^{-1} is well explained by 0–10 and 011 peaks. The peak at q_{xy}/q_z = 1.834 Å^{-1}/0.264 Å^{-1} is associated with the 100-peak arising from the π–π parallel stacking of the bdc units observed at an interplanar distance of d_{100} = 3.39 Å. Even the peak series along q_z at q_{xy} = 2.08 Å^{-1} is well reproduced by the Cu(bdc)-TF* structure. Thus, the experimental GIXD pattern is in excellent agreement with the calculated one.

The comparison is repeated for the CtM sample (see Figure 7b). As with the LbL sample, a map integrated over the azimuthal angle is used to display all diffraction peaks, since the axial texture causes the absence of certain Bragg reflections at specific orientations. In this representation, mostly Debye-Scherrer rings are observed, and the calculated diffraction pattern is overlaid by white quarter circles. The white arrow marks the 111 silicon diffraction peak, and the white triangles denote the Debye—Scherrer rings associated with the 021 and 111 $Cu(OH)_2$ diffraction maxima. The *q*-values of the Debye-Scherrer rings align well with those predicted from the theoretical crystal structure. This

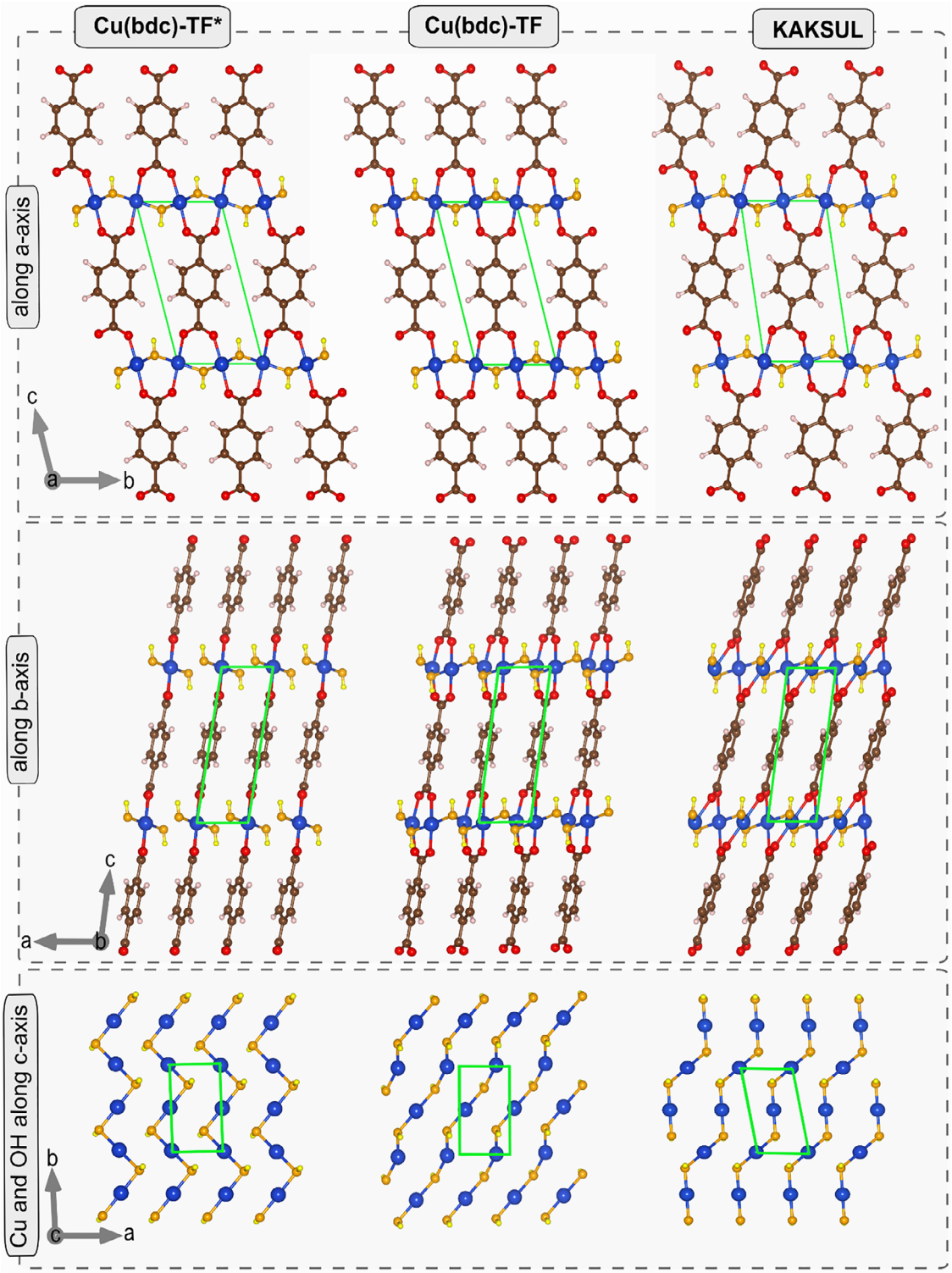

FIGURE 6 | Comparison of three possible densely packed thin-film structures of Cu(bdc): Cu(bdc)-TF*, Cu(bdc)-TF, and KAKSUL. Views along the a, b, and c axes are shown. For the views along the a and b directions, the structures are displayed with a thickness of one unit cell, while supercells are shown perpendicular to the viewing direction. When viewing along the c-direction, only the Cu^{2+} and the OH^- groups are shown to better visualize their arrangement. When viewed along the a-axis, all structures appear rather similar. The view along the b-axis clearly reveals significant differences in the alignment of the bdc linkers. In Cu(bdc)-TF and Cu(bdc)-TF*, the bdc linkers are less inclined relative to the normal to the Cu^{2+} planes. Moreover, in Cu(bdc)-TF*, there are rows of Cu^{2+} ions aligned in b-direction and, concomitantly, the O-C-O planes of the carboxylic linkers coincide with the bc-planes. The c-axis view further highlights differences in the arrangement of Cu-layers and, in particular, shows marked deviations in the structures and orientations of the Cu^{2+}-OH^--CU^{2+}-OH^- chains, which are obtained by connecting the Cu^{2+} ions to the nearest two OH-groups (see blue-orange lines). Green rectangles mark the respective unit cells. Atom colors: Cu (blue), O (red and orange), C (brown), H (white and yellow). In hydroxyl (OH^-) groups, oxygen atoms are highlighted in orange, and hydrogen atoms in yellow.

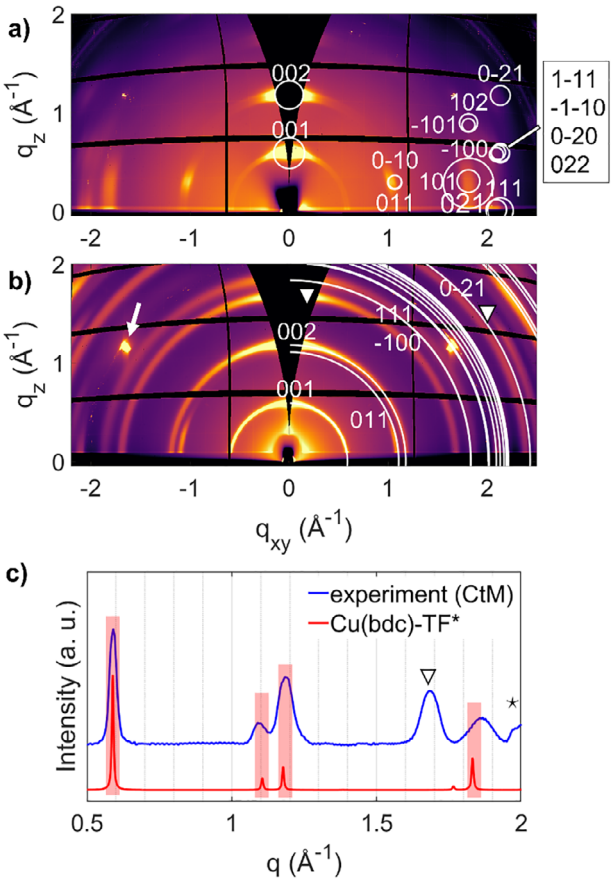

FIGURE 7 | Comparison of calculated diffraction patterns based on the fully optimized Cu(bdc)-TF* crystal structure with experimental GIXD results. (a) Reciprocal space map of the Cu(bdc) thin film grown with the layer-by-layer technique compared to the calculated 2D peak pattern. The centers and areas of the white circles represent peak positions and associated structure factors. For the sake of clarity, the calculated 2D pattern is plotted only in the right half or the panel, as the left and right half of the reciprocal space maps contain the same information. (b) Azimuthally integrated reciprocal space map of Cu(bdc) thin film grown with the ceramic-to-MOF technique compared to the calculated 2D peak pattern (white quadrants). The white arrow and the white triangle mark the silicon and the $Cu(OH)_2$ diffraction features, respectively. (c) Comparison of the simulated powder pattern of Cu(bdc)-TF*(red line) with the quasi-powder pattern of the CtM sample (blue line), including substrate peaks (denoted by ∇ and *). Vertical red bars emphasize the calculated peak positions.

agreement confirms that both the LbL and CtM thin films share the same crystal structure, and that this is consistent with that of Cu(bdc)-TF*. A comparison of the reciprocal space maps with the calculated pattern of Cu(bdc)-TF is provided for both samples in Figure S13a,b.

Also, a comparison between the measured and calculated (quasi-) powder patterns of the ceramic-to-MOF sample shown in Figure 7c confirms the appropriateness of the suggested structure. The corresponding result for Cu(bdc)-TF is contained in Figure S13c. The agreement by far exceeds that obtained for any of the structures tested above and shown in Figure 3.

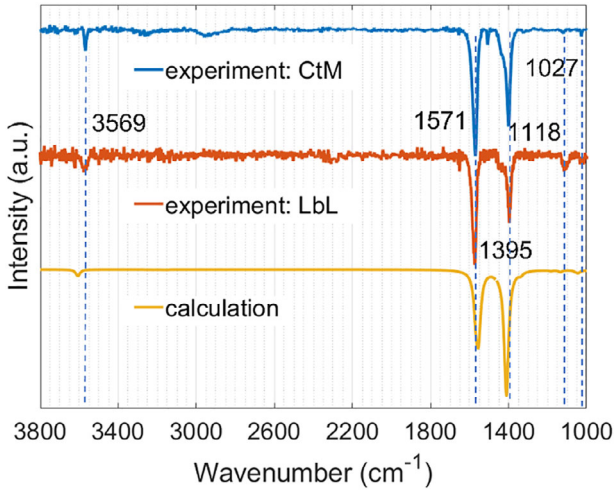

FIGURE 8 | Infrared transmission spectra of different Cu(bdc) films. The experimental spectra are presented for both the layer-by-layer (on pristine Si) and the ceramic-to-MOF samples. An excellent agreement with the calculated spectrum based on Cu(bdc)-TF* is found. The impact of absorption of the Si substrate is negligible (save the weak feature at 1118 cm^{-1} and the shoulder around 1450 cm^{-1}; see Figure S18).

As a final consistency check, the IR spectra of the CtM and LbL fabricated films were measured and compared to the results of IR simulations on the Cu(bdc)-TF* structure. Again, an excellent agreement is reached (see Figure 8), which further supports the assumed nature and arrangement of the material's building blocks. The peaks at 1571 cm^{-1} and at 1395 cm^{-1} are identified as the asymmetric, ν_{as}(COO), and symmetric, ν_s(COO), stretching modes of the carboxylates. The measured splitting of 174 cm^{-1} correlates extremely well with that calculated for the Cu(bdc)-TF* structure and is also consistent with the existing literature [28].

Even more relevant for the structural identification is the peak at 3569 cm^{-1}. As it appears in both films and in the simulations, it cannot be related to any substrate vibrations. An inspection of the eigenmodes associated with the very close-lying peak calculated to be at 3610 cm^{-1} allows associating the mode with O-H stretching vibrations. This supports the notion that -OH$^-$ groups are present in the structure. Interestingly, these vibrations have also been observed in the study revealing the ferromagnetic nature of the Cu(bdc) thin films [14]. It should also be mentioned that the correct positions of the O-H stretching modes are obtained only, when including anharmonic corrections in the simulations (see methods section). The peaks at 1027 and 1118 cm^{-1} are associated with C-H twisting and scissoring vibrations in the phenylene rings and are also consistently observed in experiments and simulations.

2.8 | Comparison to Zn-Based Terephthalate Coordination Networks

A final, interesting aspect is that the Cu(bdc)-TF* structure is reminiscent of the structure of certain Zn-based terephthalate coordination networks recently discussed by C. Leroy et al. [58]. A number of such structures have been included into the CSD, with two of them being particularly relevant for the present study.

These are the structures with the identifier ECATIO [59] and the metastable structure with the identifier PUCYAO [48]. Their chemical composition ($Zn_2(OH)_2(bdc)$) is equivalent to that of the Cu(bdc) thin film phase except for the different metal ions. Both materials represent non-porous, densely packed structures. The diffraction patterns of the PUCYAO and ECATIO structures resemble but do not match that of our LbL film (see Figure S5). Therefore, to refine the structural model, we performed simulations in which we replaced the Zn^{2+} ions from the aforementioned CSD structures by Cu^{2+} ions and fully optimized their geometries, including the lattice parameters. In the ECATIO case, this yielded a structure with a diffraction pattern essentially identical to that of the KAKSUL structure (which, as mentioned above, is reported as a Cu^{2+} based structure in the CSD). The main difference between the two structures lies in the orientation of the bdc linkers. In KAKSUL, the bdc linkers consistently align in the same direction across all layers. In ECATIO, however, the bdc linkers alternate their orientation: while in one linker layer they align similarly to KAKSUL, in the next linker layer they are rotated or crossed (see Figure S14). Notably, and in contrast to the KAKSUL case, the Cu^{2+} analogue of the ECATIO structure (Cu^{2+}-ECATIO*) represents a stable energy minimum in the simulations; at least it does not convert to Cu(bdc)-TF* in the geometry optimizations (as KAKSUL did, see Figure S12). This suggests that in cases in which the classical KAKSUL-derived diffraction pattern has been observed for Cu(bdc) type crystallites [20], the actual structure of the material could correspond to Cu^{2+}-ECATIO*. For the thin films studied here, Cu^{2+}-ECATIO* does not represent the correct solution as its diffraction patern is very close to that of the KAKSUL structure (see Figure S14b), which does not match our experiments (see above). The actual comparison of the GIXD pattern of the Cu^{2+}-ECATIO* structure to that of the LbL film is shown in Figure S16a.

Interestingly, the Cu^{2+} analogue of the second structure mentioned above, Cu^{2+}-PUCYAO*, yields a diffraction pattern strongly reminiscent of that of Cu(bdc)-TF* (see Figure S15). This similarity arises from the nearly identical arrangement of Cu-hydroxide layers and bdc linkers when viewed within the plane of the layers and along the stacking direction. However, when viewed along the direction of the bdc linkers, a key difference becomes evident: in Cu^{2+}-PUCYAO*, the orientation of the bdc linkers alternates by approximately 90° in each successive layer. This, however, does not result in discernible additional peaks that could be identified in our thin-film experiments (see Figures S15b and S16b). We attribute this to the diffraction process being dominated by the heavy metal ions and the electron densities in the linker layers not being different enough in the two structures. As a consequence, based on the available thin-film diffraction data, a prevalence of a PUCYAO-like structure in the LbL and CtM thin films cannot be excluded. In this context, the simulations also do not provide additional insight as the two structures are essentially isoenergetic (they differ by 4 meV per Cu^{2+}-PUCYAO* unit cell, which is within the error margin of the simulations). Notably, also the magnetic properties of the original structures and the structures with a doubled unit-cell length in *c*-direction (ECATIO and PUCYAO) are the same: for Cu^{2+}-ECATIO* we find an antiferromagnetic ground state (like for KAKSUL), while for the PUCYAO derivative a ferromagnetic ground state like in Cu(bdc)-TF* prevails [14]. This is also good news, as it suggests that the two possible "final" structures Cu(bdc)-TF* and Cu^{2+}-PUCYAO* have very similar physical properties.

3 | Discussion: Implications of the Cu(bdc)-TF* Structure for Functional MOF Films

A correct structural model is essential to understand the functional properties in Cu(bdc) films (e.g., guest infiltration and chemical robustness). The thin-film structure we determine (Cu(bdc)-TF*, stoichiometry $Cu_2(OH)_2(bdc)$) is compact: XRR shows an electron density about 2.6 times larger than that of 3D pillared $Cu_2(bdc)_2(dabco)$ films, and the refined triclinic cell has a much smaller volume than any porous candidate considered. These properties indicate a non-porous nature of the framework in the as-grown films.

The dense structure of Cu(bdc)-TF* explains why post-synthetic infiltration is absent for Cu(bdc) films prepared by the LbL [16] and CtM [17] techniques and why there is a need for pillared $Cu_2(bdc)_2(dabco)$ structures to reliably achieve porosity [10]. Typically, dye inclusion for Cu(bdc) occurs during MOF growth rather than through post-synthetic diffusion, which aligns with restricted access apertures throughout the film. A dense Cu(bdc)-TF* arrangement with Cu–OH chains closely linked by bdc linkers naturally blocks mass transfer, limiting guest molecule uptake. Conversely, for $Cu_2(bdc)_2(dabco)$, uniform Ag^+ infiltration is observed after simple immersion, and N_2 sorption on the detached film shows a type-I isotherm with BET $\approx$723 m^2 g^{-1}, confirming accessible microporosity [10].

The same Cu(bdc)-TF* structural features explain the chemical stability against water observed for layer-by-layer and heteroepitaxially grown Cu(bdc) films. For example, in previous reports on CtM films, in situ GIWAXS, and ex situ microscopy show that Cu(bdc) films retain crystallinity and a plate-like morphology from 50% relative humidity (RH) up to exposure to liquid water. In contrast, porous $Cu_2(bdc)_2(dabco)$ films degrade and recrystallize to Cu(bdc) at $\geq$50%–80% RH via a dissolution–reprecipitation route [17]. In the commonly assumed stacked $Cu_2(bdc)_2$ (MOF-2/SURMOF-2) model with open 1D square channels, this relative water stability of 2D films has been attributed to the small and hydrophobic pore openings perpendicular to the substrate and an interlayer spacing of ~5.8 Å that limits water ingress. However, a dense Cu(bdc)-TF* structure would be even more in line with the experimentally observed diffusion limitation and hydrolytic stability.

Finally, Zn(bdc) is often viewed as porous analogue to Cu(bdc). However, in our analysis, simply substituting Cu^{2+} for Zn^{2+} cations in MOF-2-type structures fails to reproduce the experimental quasi-powder pattern or the rotating-GIXD peak topology for thin films; in contrast, the Cu(bdc)-TF* structure is consistent with the scattering experiments, and it also reconciles the carboxylate splitting and the O-H stretch observed in the IR spectra. Also for Zn(bdc) thin-films, an in-depth analysis reveals complex structures that are different from the Cu(bdc)-TF* structure observed here. The one exception is the Zn^{2+}-based PUCYAO structure discussed in the previous section, for which the Cu^{2+} analogue (Cu^{2+}-PUCYAO*) would be consistent with

measurements on Cu(bdc) thin films. Functionally, this means that design rules based on porous Zn(bdc) MOFs cannot a priori be assumed to work for Cu(bdc) films prepared by the LbL and CtM techniques. The implications for MOF-based device fabrication are evident: (i) predictions for guest transport, sorption, or responsiveness should be determined specifically for the dense Cu(bdc)-TF* framework; (ii) the fabrication of host-guest systems for Cu(bdc) films is facilitated by in situ encapsulation; (iii) rationalizing the hydrolytic stability provides new guidelines for employing Cu(bdc) films as dense, robust frameworks.

4 | Conclusion

Combining evidence from a variety of complementary techniques, this work resolves the long-standing discussion concerning the actual crystal structure of thin films consisting of the coordination network formed when combining Cu^{2+} ions and bdc linkers. It is also discussed how the structure directly impacts the functionality of the thin films. The two films at the heart of the present study have been produced by fundamentally complementary methods: a layer-by-layer deposition approach and ceramic-to-MOF conversions. Despite the fundamentally different types of textures observed in the two thin film samples, they both display identical crystal structures. For phase identification, we apply a multi-step procedure, successively eliminating a priori plausible structural motifs: already quasi-powder spectra suffice to rule out known crystal structures of (typically) bulk Cu(bdc) from the Cambridge Structural Database. This also applies to structural arrangements suggested in literature, especially when applying DFT to fully relax the suggested structures, including unit-cell parameters. Only structures with lattice constants fixed to the outcomes of other powder-diffraction type experiments seem to provide a potential agreement with quasi-powder patterns extracted from our rotating-GIXD data. However, when considering scattering in 3D reciprocal space accessible by rotating-GIXD experiments, that is, when going beyond straightforward in- and out-of-plane scattering data, it becomes evident that neither the established structures nor related structural motifs accurately describe the entirety of the data available to us. Therefore, it is evident that an alternative approach has to be adopted, solving the crystal structure by a combined experimental/theoretical strategy. A complication at this stage is that the exact chemical composition of the studied films is a priori unknown (this refers, e.g., to the Cu^{2+} to bdc ratio and to the potential presence of OH^- groups or solvent molecules, including H_2O). A crucial ingredient for the final phase assessment was access to the textures of the two films via pole figures extracted from the rotating-GIXD data. Additionally, determining the total electron density of the samples from the critical angles of total reflection in X-ray reflectivity experiments (re)directed the search towards a densely packed structure. Indexing of the diffraction patterns, while taking the different textures into account, yielded a triclinic unit cell with lattice constants similar but not identical to the structure known by its CSD refcode as KAKSUL. Subsequently, DFT optimizations of the lattice parameters and the atomic arrangements were performed assuming a chemical composition of $Cu_2(OH)_2$(bdc) with one formula unit per unit cell (in analogy to the situation for the KAKSUL case). This yields a non-porous, densely packed structure and shows that the lattice originally extracted from the rotating-GIXD experiments corresponds to a minimum on the potential-energy surface. The identified crystal structure (i) fully explains the characteristic features of the diffraction patterns, (ii) its non-porous nature is in good agreement with the comparably high electron density observed by X-ray reflectivity, (iii) its ferromagnetic ground state is consistent with previous measurements by Friedlander et al. [14]. Moreover, (iv) the presence of OH- groups in addition to bdc^{2-} and Cu^{2+} structures matches the results of IR-absorption experiments. Overall, by combining a variety of state-of-the-art techniques, this work identifies a densely packed structure for solution grown Cu(bdc) thin films (denoted as Cu(bdc)-TF*) that is fully consistent with all available data. The absence of sufficiently large void volumes within the crystalline structure allows us to classify Cu(bdc) in thin films as a crystalline coordination network. In the discussion section, the implications of the identified Cu(bdc)-TF* structure for the functional properties of Cu(bdc) films in terms of guest loading, chemical stability, and the lack of similarity to most analogous Zn^{2+}-based systems are described. In view of the new structure identified in the current study, it is worthwhile revisiting previous experiments to check whether the current (nonporous) structural motif would also be consistent with the then observed functional materials properties.

Besides identifying the structure of Cu(bdc) thin films, we portray the advantage of using rotating-GIXD as a form of X-ray scattering that allows characterizing a large fraction of reciprocal space. Combining it with complementary experimental techniques and state-of-the-art simulations makes it a particularly powerful tool for determining reliable structures in situations in which single-crystal diffraction is not an option, including cases where the stoichiometry of the material is not a priori fully established. Given that thin-film growth can yield structures distinct from bulk single crystals [60], the present procedure offers a general route to resolve film structures and to link them to function as a prerequisite for the rational design of devices.

5 | Methodology

5.1 | Experimental Methods

The synthesis of the layer-by-layer Cu(bdc) thin film (LbL) followed the literature procedure [30, 61]: For the films on pristine Si, Cu acetate monohydrate and 1,4-benzenedicarboxylic acid (H_2bdc) were dissolved separately in absolute ethanol using ultrasonication and heating to 55°C, achieving concentrations of 1 mM (Cu) and 0.1 mM (bdc), respectively. To clean the Si substrate (1 cm by 1 cm), it was rinsed with ethanol and then exposed to a UV-Ozone plasma for 20 min. The metal precursor solution and the linker solution were alternately spin-coated onto the prepared Si substrate and rinsed with pure ethanol between the deposition steps. Each deposition cycle involved spin-coating for 10 s, using an acceleration of 500 rpm/s and reaching a maximum speed of 2000 rpm. This procedure was repeated 30 times. Substrates with functional SAMs were prepared by immersion of ethanol-rinsed 100 nm Au on Si substrates in a 0.02 mM MHDA ethanolic solution for 2 days, rinsing with ethanol and also drying with nitrogen. For that procedure, commercial Au(111) substrates (Georg Albert PVD-Beschichtungen) were employed. They were prepared by thermal evaporation of 30 nm Au (99.99%

purity) onto polished single-crystal Si(100) wafers (Silicon Sense) pre-coated with a 9 nm Ti adhesion layer. On the SAM-covered substrates, Cu(bdc) films were deposited by the standard method in analogy to what has been described above for the pristine substrates.

The synthesis of the ceramic-to-MOF Cu(bdc) thin film (CtM) followed the literature procedure described in [10, 32]: Here, crystalline $Cu(OH)_2$ nanobelts serve as precursors. They are unidirectionally injected into a water basin with a syringe to create a uniform film on the water's surface. Subsequently, the nanobelts are gently pressed onto a silicon wafer, keeping them as parallel as possible. Then they are cleaned with ethanol and dried with nitrogen. As a final step, the Cu(bdc) thin film is produced by immersing the $Cu(OH)_2$ nanobelts-coated Si substrates for ten minutes into the linker solution, composed of a 10-mL ethanol-water mixture (7.14 mL ethanol, 2.86 mL water) containing 0.1 mg/mL of H_2bdc. A more extended description of the procedure is provided in the Supporting Information [10, 32]. As substrate for the CtM samples, Si(100) from Siegert Wafer GmbH with a thickness of 675 µm, p-doped with B and an electrical resistance of 1–10 Ohm cm, was used.

Fourier transform infrared (FTIR) spectra were measured between 400 and 4000 cm^{-1} with a 2 cm^{-1} resolution using a Bruker ALPHA spectrometer in transmission mode, averaging over 64 scans. Subsequent data analysis was carried out using the *OPUS* software (version: 8.5) [62]. All presented infrared spectra (I_{tm}) were baseline-corrected by applying the following relation: $I_{tm} = \frac{I_{raw}}{I_{bl}}$, where I_{raw} is the measured intensity and I_{bl} is the baseline intensity, which was determined using the OriginPro 2021b software[55]. All measurements in transmission were performed on the samples using pristine Si wafers as substrates. Qualitatively, these were thin and lowly doped enough to transmit a sufficient amount of IR intensity. The negligible role of IR absorption features of the substrate is discussed more quantitatively in the Supporting Information: Section S7.2).

Grazing incidence X-ray diffraction [63] experiments with rotating samples (rotating-GIXD) were performed at the beamline XRD 1, Elettra, Trieste. The primary X-ray wavelength was 1.40 Å, and a Pilatus 2 M detector located 200 mm from the sample was used to detect the diffracted beam. To gather data for the entire reciprocal space, the sample was continuously rotated by 360° over 3600 s. During each 10-second interval (corresponding to a 1° rotation step), a two-dimensional diffraction image was recorded. Incident angles of 0.2° and 1° were chosen for the layer-by-layer and ceramic-to-MOF samples, respectively. Data conversion of the experimental data to reciprocal space was performed using the software *GIDVis* [34]. The experimental results are plotted as a function of the scattering vector $\vec{q}$, using $q = \frac{4\pi}{\lambda} sin\theta$. The scattering vector can be separated into an out-of-plane part (q_z) and two in-plane contributions (q_x and q_y). Due to the specific texture of the LbL sample, the associated diffractograms do not depend on the direction of the in-plane scattering vector. Thus, it is not necessary to distinguish between q_x and q_y and the in-plane scattering vector is denoted as q_{xy} and defined as $q_{xy}^2 = q_x^2 + q_y^2$. The rotating-GIXD data can be presented as 2D reciprocal space maps (e.g., intensities as a function of q_x and q_z), as reciprocal space maps integrated over a full sample rotation (integrated intensities as a function of q_{xy} and q_z), as pole figures (which represent the orientation distribution of the crystallites at a defined q—value [64]), or as a quasi-powder patterns by plotting the intensity as a function of q [34]. Notably, the quasi-powder patterns do not allow a fully quantitative comparison between experimental and calculated peak intensities, as some information is lost due to geometrical factors. These include, for example, the experimentally inaccessible part of q-space (like the missing wedge) and blind spots of the detector.

For comparison to measured data, diffraction patterns are also calculated using crystal structure information files (cif-files) as input. Calculated intensities are represented in two ways: for comparison with reciprocal space maps, Bragg peak intensities are visualized via structure factors, which are calculated by using the GIDVis software [34]. In contrast, the comparison of quasi-powder plots is done with simulated powder patterns generated using *Mercury, Cambridge Crystallographic Data Centre (CCDC) (version 4.3.1)*. These simulations are based on a conventional diffractometer geometry, including geometrical factors like the Lorentz-polarization and peak multiplicity.

X-ray reflectivity (XRR) measurements were performed with a PANalytical Empyrean diffractometer in specular geometry using CuKα radiation at a wavelength of $\lambda = 1.542$ Å. The primary side was equipped with a sealed copper tube and a multilayer mirror for generating a parallel beam. On the secondary side, a 0.1 mm anti-scatter slit and a 0.02 rad Soller slit were used together with a PANalytical PIXcel 3D detector working as a point detector. According to Pietsch et al., [49], critical angles of total external reflection α_C are given by the value of the angle α, at which the observed intensity drops to half of its maximum value in the region of total external reflection [49]. The electron density of the sample, ρ_e, can then be calculated from α_C by using $\alpha_C = \sqrt{2\delta}$ with $\delta = \frac{\lambda^2}{4\pi} \cdot r_e \cdot \rho_e$. Here, r_e is the classical electron radius, also denoted as Thomson scattering length [65].

5.2 | Computational Details

To generate optimized structures for all systems, the FHI-aims [66–69] code was used, combining the PBE [70] functional with a nonlocal variant of the many-body dispersion correction [71]. In the Supporting Information, Section S1 presents a detailed description of the chosen computational settings. A central element for the current study is the optimization of structural parameters of potential candidate structures of Cu(bdc). Depending on the specific target structure, either only atomic positions were relaxed or lattice parameters and atomic positions were relaxed simultaneously until the residual maximum forces dropped to below 10^{-4} eV•Å^{-1}. This is described in more detail, including the nomenclature used for the two optimization scenarios, in Section 2.1. When performing full geometry optimizations, it is possible to assess whether a specific set of lattice parameters represents a stable configuration or not. Fixed unit-cell parameters are used for test purposes, when relying on structures from the CSD or, in some cases, when referring directly to parameters extracted from rotating-GIXD data.

To simulate the infrared (IR) spectrum of Cu(bdc), we employed the CRYSTAL23 [72] software with a TZVP [73] basis set and the

B3LYP hybrid functional with D3 dispersion correction [74, 75] (see Supporting Information for full details). The relaxed lattice parameters obtained following the procedure described in the previous paragraph were used as inputs for CRYSTAL23, and, before calculating the spectra, only the atomic positions were relaxed to account for the modified computational settings when using the CRYSTAL code. The XLGRID (extra-large grid) option, which uses a dense radial–angular grid, was used to ensure accurate integration of the exchange–correlation potential, which is important for computing vibrational properties. Frequencies were obtained using numerical derivatives; anharmonic corrections for predominantly hydrogen-involving vibrations were applied [76–78].

Acknowledgements

The authors thank Jan Fischer (Karlsruhe Institute of Technology, Institute of Microstructure Technology) for preparing the LbL film on the pristine Si substrate. This research was funded in whole, or in part, by the Austrian Science Fund (FWF) [10.55776/P34463]*. For the purpose of open access, the authors have applied a CC BY public copyright license to any Author Accepted Manuscript version arising from this submission. The authors thank the Graz University of Technology [Lead Project LP-03: Porous Materials @ Work for Sustainability] for financial support. The authors acknowledge support from the European Research Council under the European Union's Horizon 2020 Programme (FP/2014-2020)/ERC Grant Agreement No. 771834—POPCRYSTAL. The authors acknowledge Elettra Synchrotron Trieste for allocating beamtime at beamline XRD1, they thank Bartolomeo Civalleri from the University of Turin for support with the IR simulations, and they gratefully acknowledge Dr. Nina Vankova (Technische Universität Dresden, Theoretical Chemistry Chair) for kindly providing the Zn-based structure model related to the system reported in [12].

Open Access funding provided by Technische Universität Graz.

Conflicts of Interest

The authors declare no conflicts of interest.

Data Availability Statement

All original data can be accessed via the repository of the Graz University of Technology. The experimental data and all.cif files can be found at https://doi.org/10.3217/crdx4-tbh40). The relevant input and output files of the simulations are provided at https://doi.org/10.3217/q4wnr-fzz25.

References

1. H. Furukawa, K. E. Cordova, M. O'Keeffe, and O. M. Yaghi, "The Chemistry and Applications of Metal-Organic Frameworks," *Science* 341, no. 6149 (2013): 1230444, https://doi.org/10.1126/science.1230444.

2. A. Felix Sahayaraj, H. Joy Prabu, J. Maniraj, et al., "Metal–Organic Frameworks (MOFs): The Next Generation of Materials for Catalysis, Gas Storage, and Separation," *Journal of Inorganic and Organometallic Polymers and Materials* 33 (2023): 1757–1781, https://doi.org/10.1007/s10904-023-02657-1.

3. L. Jiao and H.-L. Jiang, "Metal-Organic Frameworks for Catalysis: Fundamentals and Future Prospects," *Chinese Journal of Catalysis* 45 (2023): 1–5, https://doi.org/10.1016/S1872-2067(22)64193-7.

4. H. D. Lawson, S. P. Walton, and C. Chan, "Metal–Organic Frameworks for Drug Delivery: A Design Perspective," *ACS Applied Materials & Interfaces* 13, no. 6 (2021): 7004–7020, https://doi.org/10.1021/acsami.1c01089.

5. J. F. Olorunyomi, S. T. Geh, R. A. Caruso, and C. M. Doherty, "Metal–Organic Frameworks for Chemical Sensing Devices," *Materials Horizons* 8, no. 9 (2021): 2387–2419, https://doi.org/10.1039/D1MH00609F.

6. Z. Ji, H. Wang, S. Canossa, S. Wuttke, and O. M. Yaghi, "Pore Chemistry of Metal–Organic Frameworks," *Advanced Functional Materials* 30, no. 41 (2020): 2000238, https://doi.org/10.1002/adfm.202000238.

7. P. Falcaro, R. Ricco, M. Doherty, K. Liang, J. Hill, and J. Styles, "MOF Positioning Technology and Device Fabrication," *Chemical Society Reviews* 43, no. 16 (2014): 5513–5560, https://doi.org/10.1039/C4CS00089G.

8. H. Li, M. Eddaoudi, T. L. Groy, and O. M. Yaghi, "Establishing Microporosity in Open Metal–Organic Frameworks: Gas Sorption Isotherms for Zn(BDC) (BDC = 1,4-Benzenedicarboxylate)," *Journal of the American Chemical Society* 120, no. 33 (1998): 8571–8572, https://doi.org/10.1021/ja981669x.

9. J. Liu, B. Lukose, O. Shekhah, et al., "A Novel Series of Isoreticular Metal Organic Frameworks: Realizing Metastable Structures by Liquid Phase Epitaxy," *Scientific Reports* 2, no. 1 (2012): 921, https://doi.org/10.1038/srep00921.

10. P. Falcaro, K. Okada, T. Hara, et al., "Centimetre-scale micropore alignment in oriented polycrystalline metal–organic framework films via heteroepitaxial growth," *Nature materials* 16, no. 3 (2017): 342–348, https://doi.org/10.1038/nmat4815.

11. T. Stassin, S. Rodríguez-Hermida, B. Schrode, et al., "Vapour-Phase Deposition Of Oriented Copper Dicarboxylate Metal–Organic Framework Thin Films," *Chemical Communications* 55, no. 68 (2019): 10056–10059, https://doi.org/10.1039/C9CC05161A.

12. A. C. Elder, A. B. Aleksandrov, S. Nair, and T. M. Orlando, "Interactions on External MOF Surfaces: Desorption of Water and Ethanol from CuBDC Nanosheets," *Langmuir* 33, no. 39 (2017): 10153–10160, https://doi.org/10.1021/acs.langmuir.7b01987.

13. S. Kumar, Y. Pramudya, K. Müller, et al., "Sensing Molecules With Metal–Organic Framework Functionalized Graphene Transistors," *Advanced Materials* 33, no. 43 (2021): 2103316, https://doi.org/10.1002/adma.202103316.

14. S. Friedländer, J. Liu, M. Addicoat, et al., "Linear Chains of Magnetic Ions Stacked With Variable Distance: Ferromagnetic Ordering With a Curie Temperature Above 20 K," *Angewandte Chemie International Edition* 55, no. 41 (2016): 12683–12687, https://doi.org/10.1002/anie.201606016.

15. A. Nefedov, C. Li, K. Müller, et al., "Magnetic Coupling of Guest Metallocene Molecules with SURMOF-2 Host Matrix," *Physical Review B* 107, no. 5 (2023): 054433, https://doi.org/10.1103/PhysRevB.107.054433.

16. B. D. Dhanapala, D. L. Maglich, and M. E. Anderson, "Impact of Surface Functionalization and Deposition Method on Cu-BDC surMOF Formation, Morphology, Crystallinity, and Stability," *Langmuir* 39, no. 34 (2023): 12196–12205, https://doi.org/10.1021/acs.langmuir.3c01505.

17. L. A. Brandner, M. Linares-Moreau, G. Zhou, et al., "Water Sensitivity of Heteroepitaxial Cu-MOF Films: Dissolution and Re-Crystallization of 3D-Oriented MOF Superstructures," *Chemical Science* 14, no. 43 (2023): 12056–12067, https://doi.org/10.1039/D3SC04135B.

18. C. G. Carson, G. Brunnello, S. G. Lee, S. S. Jang, R. A. Gerhardt, and R. Tannenbaum, "Structure Solution From Powder Diffraction of Copper 1,4-Benzenedicarboxylate," *European Journal of Inorganic Chemistry* 2014, no. 12 (2014): 2140–2145, https://doi.org/10.1002/ejic.201301543.

19. B. M. Omkaramurthy and G. Krishnamurthy, "Synthesis and Characterization of Mesoporous Crystalline Copper Metal–Organic Frameworks for Electrochemical Energy Storage Application," *SN Applied Sciences* 2, no. 3 (2020): 342, https://doi.org/10.1007/s42452-020-2051-6.

20. S. Abdelouhab, M. François, E. Elkaim, and P. Rabu, "Ab Initio Crystal Structure of Copper (II) Hydroxy-Terephthalate by Synchrotron Powder Diffraction and Magnetic Properties," *Solid state Sciences* 7, no. 2 (2005): 227–232, https://doi.org/10.1016/j.solidstatesciences.2004.10.020.

21. J. Multia, D. E. Kravchenko, V. Rubio-Giménez, A. Philip, R. Ameloot, and M. Karppinen, "Nanoporous Metal–Organic Framework Thin Films

Prepared Directly From Gaseous Precursors by Atomic and Molecular Layer Deposition: Implications for Microelectronics," *ACS Applied Nano Materials* 6, no. 2 (2023): 827–831, https://doi.org/10.1021/acsanm.2c04934.

22. V. Rubio-Giménez, F. Carraro, S. Hofer, et al., "Polymorphism and Orientation Control Of Copper-Dicarboxylate Metal–Organic Framework Thin Films Through Vapour- And Liquid-Phase Growth," *CrystEngComm* 26, no. 8 (2024): 1071–1076, https://doi.org/10.1039/D3CE01296D.

23. L. Deakin, A. M. Arif, and J. S. Miller, "Observation of Ferromagnetic and Antiferromagnetic Coupling in 1-D and 2-D Extended Structures of Copper (II) Terephthalates," *Inorganic Chemistry* 38 (1999): 5072–5077, https://doi.org/10.1021/ic990400r.

24. H. Li, M. Eddaoudi, T. L. Groy, and O. M. Yaghi, "Establishing Microporosity in Open Metal-Organic Frameworks: Gas Sorption Isotherms for Zn (BDC)(BDC = 1, 4-Benzenedicarboxylate)," *Journal of the American Chemical Society* 120, no. 33 (1998): 8571–8572, https://doi.org/10.1021/ja981669x.

25. C. G. Carson, K. Hardcastle, and J. Schwartz, *Synthesis and Structure Characterization of Copper Terephthalate Metal–Organic Frameworks* (Wiley Online Library, 2009), https://doi.org/10.1002/ejic.200801224.

26. P. J. Hay and J. C. Thibeault, "Orbital Interactions in Metal Dimer Complexes," *Journal of the American Chemical Society* 97, no. 17 (1975): 4884–4899, https://doi.org/10.1021/ja00850a018.

27. S. Petkov, G. N, J. Liu, et al., "Defects in MOFs: A Thorough Characterization," *ChemPhysChem* 13, no. 8 (2012): 2025–2029, https://doi.org/10.1002/cphc.201200222.

28. B. Baumgartner, K. Ikigaki, K. Okada, and M. Takahashi, "Infrared Crystallography for Framework and Linker Orientation in Metal–Organic Framework Films," *Chemical Science* 12, no. 27 (2021): 9298–9308, https://doi.org/10.1039/D1SC02370E.

29. M. Fratschko, T. Zhao, J. C. Fischer, O. Werzer, F. Gasser, and I. A. Howard, "Thin Film Formation Based on a Nanoporous Metal–Organic Framework by Layer-By-Layer Deposition," *ACS Applied Nano Materials* 7, no. 22 (2024): 25645–25654, https://doi.org/10.1021/acsanm.4c04763.

30. J. C. Fischer, R. Steentjes, D. Chen, B. S. Richards, E. Zojer, and C. Wöll, "Determining Structures of Layer-by-Layer Spin-Coated Zinc Dicarboxylate-Based Metal-Organic Thin Films," *Chemistry—A European Journal* 30, no. 37 (2024): 202400565, https://doi.org/10.1002/chem.202400565.

31. O. Shekhah, "Layer-by-Layer Method for the Synthesis and Growth of Surface Mounted Metal-Organic Frameworks (SURMOFs)," *Materials* 3, no. 2 (2010): 1302–1315, https://doi.org/10.3390/ma3021302.

32. M. Linares-Moreau, L. A. Brandner, T. Kamencek, et al., "Semi-Automatic Deposition of Oriented $Cu(OH)_2$ Nanobelts for the Heteroepitaxial Growth of Metal–Organic Framework Films," *Advanced Materials Interfaces* 8, no. 21 (2021): 2101039, https://doi.org/10.1002/admi.202101039.

33. V. Chernikova, O. Shekhah, and M. Eddaoudi, "Advanced Fabrication Method for the Preparation of MOF Thin Films: Liquid-Phase Epitaxy Approach Meets Spin Coating Method," *ACS Applied Materials & Interfaces* 8, no. 31 (2016): 20459–20464, https://doi.org/10.1021/acsami.6b04701.

34. B. Schrode, S. Pachmajer, M. Dohr, et al., "GIDVis: A Comprehensive Software Tool for Geometry-Independent Grazing-Incidence X-Ray Diffraction Data Analysis and Pole-Figure Calculations," *Journal of Applied Crystallography* 52, no. 3 (2019): 683–689, https://doi.org/10.1107/S1600576719004485.

35. M. Fratschko, N. Strasser, N. Taghizade, et al., "Identifying Structure and Texture of Metal–Organic Framework Cu_2 $(bdc)_2$ (dabco) Thin Films by Combining X-ray Diffraction and Quantum Mechanical Modeling," *Crystal Growth & Design* 25 (2025): 3665–3679, https://doi.org/10.1021/acs.cgd.4c01433.

36. E. Parsianpour, D. Raoufi, M. Roostaei, B. Sohrabi, and F. Samavat, "Characterization and Structural Property of Indium Tin Oxide Thin Films," *Advances in Materials Physics and Chemistry* 07, no. 02 (2017): 42–57, https://doi.org/10.4236/ampc.2017.72005.

37. H. von Jaggi and H. R. Oswald, "Die Kristallstruktur Des Kupferhydroxids $Cu(OH)_2$," *Acta Crystallographica* 14, no. 10 (1961): 1041–1045, https://doi.org/10.1107/S036511061003016.

38. H. R. Oswald, A. Reller, H. W. Schmalle, and E. Dubler, "Structure of Copper(II) Hydroxide, $Cu(OH)_2$," *Acta Crystallographica Section C Crystal Structure Communications* 46, no. 12 (1990): 2279–2284, https://doi.org/10.1107/S0108270190006230.

39. P. Niggli, *Krystallographische Und Strukturtheoretische Grundbegriffe* (Akademische verlagsgesellschaft mbh 1928).

40. Y. Zhang, M. Položij, and T. Heine, "Statistical Representation of Stacking Disorder in Layered Covalent Organic Frameworks," *Chemistry of Materials* 34, no. 5 (2022): 2376–2381, https://doi.org/10.1021/acs.chemmater.1c04365.

41. R. Steentjes and E. Zojer, "The Dynamics of Stacking in Layered Covalent Organic Frameworks," *Monatshefte für Chemie—Chemical Monthly* 157 (2025): 401–414, https://doi.org/10.1007/s00706-025-03412-7.

42. A. O. F. Jones, B. Chattopadhyay, Y. H. Geerts, and R. Resel, "Substrate-Induced and Thin-Film Phases: Polymorphism of Organic Materials on Surfaces," *Advanced Functional Materials* 26, no. 14 (2016): 2233–2255, https://doi.org/10.1002/adfm.201503169.

43. E. Zojer, "Maximizing the Carrier Mobilities of Metal–Organic Frameworks Comprising Stacked Pentacene Units," *Journal of Physical Chemistry Letters* 12, no. 29 (2021): 7002–7009, https://doi.org/10.1021/acs.jpclett.1c01892.

44. L. Legenstein, S. Rodríguez-Hermida, V. Rubio-Giménez, et al., "Identifying the Internal Network Structure of a New Copper Isonicotinate Thin-Film Polymorph Obtained via Chemical Vapor Deposition," *Advanced Materials Interfaces* 10 (2023): 2202461, https://doi.org/10.1002/admi.202202461.

45. C. J. Heffelfinger and R. L. Burton, "X-Ray Determination of the Crystallite Orientation Distributions of Polyethylene Terephthalate Films," *Journal of Polymer Science* 47, no. 149 (1960): 289–306, https://doi.org/10.1002/pol.1960.1204714926.

46. S. Hofer, W. Bodlos, J. Novák, A. Sanzone, L. Beverina, and R. Resel, "Molecular Packing Analysis of the Crystal Smectic E Phase of a Benzothieno-Benzothiophene Derivative by a Combined Experimental/Computational Approach," *Liquid Crystals* 48, no. 13 (2021): 1888–1896, https://doi.org/10.1080/02678292.2021.1907626.

47. A. Pichler, R. Resel, A. Neuhold, et al., "Crystal Structure Determination of Organic Thin-Films: The Example of 2,2′: 6′,2″-Ternaphthalene," *Zeitschrift für Kristallographie—Crystalline Materials* 229 (2014): 385–393, https://doi.org/10.1515/zkri-2013-1704.

48. A. Carton, A. Mesbah, L. Aranda, P. Rabu, and M. François, "New Metastable Hybrid Phase, $Zn_2(OH)_2(C_8H_4O_4)$, Exhibiting Unique Oxo-Penta-Coordinated Zn(II) Atoms," *Solid State Sciences* 11 (2009): 818–823, https://doi.org/10.1016/j.solidstatesciences.2008.12.011.

49. U. Pietsch, V. Holy, and T. Baumbach, *High-Resolution X-Ray Scattering: From Thin Films to Lateral Nanostructures* (Springer Science & Business Media, 2004).

50. A. Naudon and D. Thiaudiere, "Grazing-Incidence Small-Angle Scattering. Morphology of Deposited Clusters and Nanostructure of Thin Films," *Journal of Applied Crystallography* 30, no. 5 (1997): 822–827, https://doi.org/10.1107/S002188989700099X.

51. A. S. Lenshin, Y. A. Peshkov, M. V. Grechkina, S. V. Kannykin, and Y. A. Yurakov, "X-Ray Reflectivity Investigation of Multilayer Macroporous Silicon Structures," *Journal of Physics: Conference Series* 1984, no. 1 (2021): 012018, https://doi.org/10.1088/1742-6596/1984/1/012018.

52. M. Tazreiter, "Error Analysis for X-Ray Reflectivity: An Experimental Series," (Bachelor thesis, Graz University of Technology, 2014).

53. J. C. Fischer, C. Li, S. Hamer, et al., "GIWAXS Characterization of Metal–Organic Framework Thin Films and Heterostructures: Quantifying Structure and Orientation," *Advanced Materials Interfaces* 10, no. 11 (2023): 2202259, https://doi.org/10.1002/admi.202202259.

54. J. B. Goodenough, "Theory of the Role of Covalence in the Perovskite-Type Manganites [La, *M* (II)] Mn O_3," *Physical Review* 100 (1955): 564, https://doi.org/10.1103/PhysRev.100.564.

55. J. B. Goodenough, "An interpretation of the magnetic properties of the perovskite-type mixed crystals La1-xSrxCoO3-λ," *Journal of Physics and Chemistry of Solids* 6, no. 23, (1958): 287–297, https://doi.org/10.1016/0022-3697(58)90107-0.

56. J. Kanamori, "Superexchange Interaction and Symmetry Properties of Electron Orbitals," *Journal of Physics and Chemistry of Solids* 10, no. 2–3 (1959): 87–98, https://doi.org/10.1016/0022-3697(59)90061-7.

57. J. B. Goodenough, "An Interpretation of the Magnetic Properties of the Perovskite-Type Mixed Crystals $La_{1-x}Sr_xCoO_{3-\lambda}$," *Journal of Physics and Chemistry of Solids*6, no. 2–3 (1958): 287–297, https://doi.org/10.1016/0022-3697(58)90107-0.

58. C. Leroy, T.-X. Métro, I. Hung, Z. Gan, C. Gervais, and D. Laurencin, "From Operando Raman Mechanochemistry to "NMR Crystallography": Understanding the Structures and Interconversion of Zn-Terephthalate Networks Using Selective17 O-Labeling," *Chemistry of Materials* 34, no. 5 (2022): 2292–2312, https://doi.org/10.1021/acs.chemmater.1c04132.

59. J. A. Kaduk, "CCDC 1520407: Experimental Crystal Structure Determination," (2016), https://doi.org/10.5517/CCDC.CSD.CC1N13D6.

60. O. Shekhah, H. Wang, M. Paradinas, et al., "Controlling Interpenetration In Metal–Organic Frameworks By Liquid-Phase Epitaxy," *Nature Materials* 8, no. 6 (2009): 481–484, https://doi.org/10.1038/nmat2445.

61. R. Haldar, M. Jakoby, A. Mazel, et al., "Anisotropic Energy Transfer in Crystalline Chromophore Assemblies," *Nature Communications* 9, no. 1 (2018): 4332, https://doi.org/10.1038/s41467-018-06829-3.

62. M. L. Adelberg, R. I. DeVries, Z. A. Moschovidis, and L. Razgunas, *Opus: A Programming System Approach to Structural Optimization* (SAE Technical Paper, 1981), https://doi.org/10.4271/811316.

63. O. Werzer, S. Kowarik, F. Gasser, et al., "X-Ray Diffraction under Grazing Incidence Conditions," *Nature Reviews Methods Primers* 4 (2024): 15, https://doi.org/10.1038/s43586-024-00293-8.

64. K. Nagao and E. Kagami, "X-Ray Thin Film Measurement Techniques VII. Pole Figure Measurement," *Rigaku Journal* 27(2011): 6–14.

65. J. Als-Nielsen and D. McMorrow, *Elements of Modern X-Ray Physics* (John Wiley & Sons, 2011), https://doi.org/10.1002/9781119998365.

66. V. Blum, R. Gehrke, F. Hanke, et al., "Ab Initio Molecular Simulations with Numeric Atom-Centered Orbitals," *Computer Physics Communications* 180, no. 11 (2009): 2175–2196, https://doi.org/10.1016/j.cpc.2009.06.022.

67. V. Blum, M. Rossi, S. Kokott, and M. Scheffler, "The FHI-Aims Code: All-Electron, Ab Initio Materials Simulations towards the Exascale," *arXiv* (2022), https://doi.org/10.48550/arXiv.2208.12335.

68. V. Havu, V. Blum, P. Havu, and M. Scheffler, "Efficient O(N) Integration for all-Electron Electronic Structure Calculation Using Numeric Basis Functions," *Journal of Computational Physics* 228, no. 22 (2009): 8367–8379, https://doi.org/10.1016/j.jcp.2009.08.008.

69. A. Marek, V. Blum, R. Johanni, et al., "The ELPA Library: Scalable Parallel Eigenvalue Solutions for Electronic Structure Theory and Computational Science," *Journal of Physics: Condensed Matter* 26, no. 21 (2014): 213201, https://doi.org/10.1088/0953-8984/26/21/213201.

70. J. P. Perdew, K. Burke, and M. Ernzerhof, "Generalized Gradient Approximation Made Simple," *Physical Review Letters* 77, no. 18 (1996): 3865–3868, https://doi.org/10.1103/PhysRevLett.77.3865.

71. A. Tkatchenko, R. A. DiStasio Jr, R. Car, and M. Scheffler, "Accurate and Efficient Method for Many-Body van Der Waals Interactions," *Physical Review Letters* 108, no. 23 (2012): 236402, https://doi.org/10.1103/PhysRevLett.108.236402.

72. A. Erba, J. K. Desmarais, S. Casassa, et al., "CRYSTAL23: A Program for Computational Solid State Physics and Chemistry," *Journal of Chemical Theory and Computation* 19 (2023): 6891–6932, https://doi.org/10.1021/acs.jctc.2c00958.

73. A. Schäfer, C. Huber, and R. Ahlrichs, "Fully Optimized Contracted Gaussian Basis Sets of Triple Zeta Valence Quality for Atoms Li to Kr," *Journal of Chemical Physics* 100, no. 8 (1994): 5829–5835, https://doi.org/10.1063/1.467146.

74. A. D. Becke, "Density-functional Thermochemistry. I. The Effect of the Exchange-only Gradient Correction," *Journal of Chemical Physics* 96, no. 3 (1992): 2155–2160, https://doi.org/10.1063/1.462066.

75. S. Grimme, J. Antony, S. Ehrlich, and H. Krieg, "A Consistent and Accurate Ab Initio Parametrization of Density Functional Dispersion Correction (DFT-D) for the 94 Elements H-Pu," *Journal of Chemical Physics* 132 (2010): 154104, https://doi.org/10.1063/1.3382344.

76. A. Erba, J. Maul, M. Ferrabone, P. Carbonnière, M. Rérat, and R. Dovesi, "Anharmonic Vibrational States of Solids from DFT Calculations. Part I: Description of the Potential Energy Surface," *Journal of Chemical Theory and Computation* 15, no. 6 (2019): 3755–3765, https://doi.org/10.1021/acs.jctc.9b00293.

77. A. Erba, J. Maul, M. Ferrabone, R. Dovesi, M. Rérat, and P. Carbonnière, "Anharmonic Vibrational States of Solids from DFT Calculations. Part II: Implementation of the VSCF and VCI Methods," *Journal of Chemical Theory and Computation* 15, no. 6 (2019): 3766–3777, https://doi.org/10.1021/acs.jctc.9b00294.

78. F. Pascale, S. Tosoni, C. Zicovich-Wilson, P. Ugliengo, R. Orlando, and R. Dovesi, "Vibrational Spectrum of Brucite, $Mg(OH)_2$: a Periodic ab initio Quantum Mechanical Calculation Including OH Anharmonicity," *Chemical Physics Letters* 396, no. 4–6 (2004): 308–315, https://doi.org/10.1016/j.cplett.2004.08.047.

Supporting Information

Additional supporting information can be found online in the Supporting Information section.

Supporting File: adfm76075-sup-0001-SuppMat.pdf.